WRF-GC (v2.0): online two-way coupling of WRF (v3.9.1.1) and GEOS-Chem (v12.7.2) for modeling regional atmospheric chemistry-meteorology interactions

Xu Feng[1], Haipeng Lin[2], Tzung-May Fu[3,4*], Melissa P. Sulprizio[2], Jiawei Zhuang[2], Daniel J. Jacob[2], Heng Tian[1], Yaping Ma[5], Lijuan Zhang[1], Xiaolin Wang[1], and Qi Chen[6]

[1]Department of Atmospheric and Oceanic Sciences, School of Physics, Peking University, Beijing, China
[2]John A. Paulson School of Engineering and Applied Sciences, Harvard University, Cambridge, Massachusetts, USA
[3]State Environmental Protection Key Laboratory of Integrated Surface Water-Groundwater Pollution Control, School of Environmental Science and Engineering, Southern University of Science and Technology, Shenzhen, Guangdong, China
[4]Shenzhen Institute of Sustainable Development, Southern University of Science and Technology, Shenzhen, Guangdong, China
[5]National Meteorological Information Center, China Meteorological Administration, Beijing, China
[6]State Key Joint Laboratory of Environmental Simulation and Pollution Control, College of Environmental Sciences and Engineering, Peking University, Beijing, China

Correspondence: Tzung-May Fu (fuzm@sustech.edu.cn)

Abstract. We present the WRF-GC model v2.0, an online two-way coupling of the Weather Research and Forecasting (WRF) meteorological model (v3.9.1.1) and the GEOS-Chem chemical model (v12.7.2). WRF-GC v2.0 is built on the modular framework of WRF-GC v1.0 and further includes aerosol-radiation interactions (ARI) and aerosol-cloud interactions (ACI) based on bulk aerosol mass and composition, as well as the capability to nest multiple domains for high-resolution simulations. WRF-GC v2.0 is the first implementation of the GEOS-Chem model in an open-source dynamic model with chemical feedbacks to meteorology. We apply prescribed size distributions to the 10 aerosol types simulated by GEOS-Chem to diagnose aerosol optical properties and activated cloud droplet numbers; the results are passed to the WRF model for radiative and cloud microphysics calculations. We use WRF-GC v2.0 to conduct sensitivity simulations with different combinations of ARI and ACI over China during January 2015 and July 2016, with the goal of evaluating the simulated aerosol and cloud properties and the impacts of ARI and ACI on meteorology and air quality. WRF-GC reproduces the day-to-day variability of the aerosol optical depth (AOD) observed by the Aerosol Robotic Network (AERONET) project at four representative Chinese sites in January 2015, with temporal correlation coefficients of 0.56 to 0.85. The magnitudes and spatial distributions of the simulated liquid cloud effective radii, liquid cloud optical depths, surface downward shortwave radiation, and surface temperature over China

for July 2016 are in good agreement with aircraft, satellite, and surface observations. WRF-GC simulations including both ARI

15 and ACI reproduce the observed surface concentrations and spatial distributions of $PM_{2.5}$ in January 2015 (normalized mean

bias = -6.6 %, spatial correlation r = 0.74) and afternoon ozone in July 2016 (normalized mean bias = 19 %, spatial correlation

r = 0.56) over Eastern China, respectively. Our sensitivity simulations show that including the ARI and ACI improved the

model's performance in simulating ozone concentrations over China in July, 2016. WRF-GC v2.0 is open source and freely

available from http://wrf.geos-chem.org.

1   Introduction

Interactions between atmospheric constituents and meteorological processes greatly impact regional weather and atmospheric

chemistry (Zhang, 2008; Baklanov et al., 2014). Meteorological conditions affect the emissions of chemical constituents into

the atmosphere from natural and anthropogenic sources, as well as the subsequent chemical reactions, transport, and removal of

those atmospheric constituents (Zhang et al., 2013; Zheng et al., 2015; Abel et al., 2017; Ma et al., 2020). In turn, atmospheric

25 aerosols can exert radiative forcings either directly by scattering or absorption of solar and terrestrial radiation (i.e., aerosol-

radiation interactions, ARI), or indirectly by altering the microphysical properties of clouds (i.e., aerosol-cloud interactions,

ACI) (Hansen et al., 1997; Haywood and Boucher, 2000; Johnson et al., 2004; Lohmann and Feichter, 2005). Many studies

have demonstrated that in areas with high aerosol concentrations, ARI and ACI can induce complex feedbacks to significantly

affect both regional meteorology and air quality (Li et al., 2007; Forkel et al., 2012; Ding et al., 2013; Wang et al., 2014a;

30 Gong et al., 2015; Tao et al., 2015; Petaja et al., 2016; Li et al., 2017b; Zhao et al., 2017). We previously developed WRF-GC

v1.0 (Lin et al., 2020a), an one-way online coupling of the WRF (Skamarock et al., 2008, 2019) meteorological model and

the GEOS-Chem (Bey et al., 2001) chemical model for simulating regional air quality without aerosol feedbacks. Here, we

present the development of WRF-GC v2.0, which further includes ARI, ACI, and nested-domain capabilities to better simulate

interactions between regional meteorology and air quality at high resolution.

35   The coupling between meteorological and chemical processes in regional models is typically achieved by one of two method-

ologies: *online-access coupling* or *online-integrated coupling* (Baklanov et al., 2014). Under the online-access coupling frame-

work, a meteorological model and a chemical transport model (CTM) separately simulate regional meteorology and atmospheric chemistry. At regular time intervals during run-time, they exchange meteorological and chemical data interpolated to the other model's grids and time to drive subsequent calculations. The meteorological model and the CTM may work with different map projections and 3-D grids, and they may use different transport schemes for meteorological and chemical variables.

40 A number of two-way models are coupled using the online-access approach, including for example the online WRF-CMAQ model (Byun and Schere, 2006; Wong et al., 2012; Yu et al., 2014), the GEM-AQ model (Kaminski et al., 2008), the COSMO-MUSCAT model (Wolke et al., 2004; Renner and Wolke, 2010), and the IFS-MOZART model (Flemming et al., 2009). In many online-access models, the CTMs can also be driven by offline meteorological data to stand alone. As such, these stand-

45 alone CTMs may be independently developed by a wider atmospheric chemistry community, and the resulting CTM advances may be quickly incorporated into the coupled model via the online-access structure (Yu et al., 2014).

Alternatively, regional coupled models may adopt an online-integrated structure, where the chemical module is an internal component of the coupled model. This structure entails meteorological and chemical calculations be performed on the same grids with the same time-stepping system. A major advantage of the online-integrated models is that meteorological and

50 chemical data do not need to be interpolated in time or space for the coupling. Also, the transport schemes for meteorological and chemical quantities are generally consistent in online-integrated models, which better ensures mass-conservation (Zhang, 2008). An example of the online-integrated coupled structure is the WRF-Chem model (Grell et al., 2005; Fast et al., 2006), which consists of the WRF model and a chemical module called by WRF at each chemical time step. The WRF-Chem model includes options to turn on ARI and ACI, either individually and combined. WRF-Chem has been widely used to study regional

55 air quality, meteorology, and their interactions (Zhang et al., 2010; Huang et al., 2016; Archer-Nicholls et al., 2016; Zhang et al., 2018). However, the chemical module in WRF-Chem cannot stand alone as a CTM.

The WRF-GC model was developed using the online-integrated structure, with WRF calling the GEOS-Chem as an internal chemical module (Lin et al., 2020a). At the same time, the GEOS-Chem model can stand alone as an offline CTM and has been actively developed by the atmospheric chemistry community (Bey et al., 2001; Eastham et al., 2018). This architecture of the

60 WRF-GC model was made possible by the recent "modularization" of the GEOS-Chem model. GEOS-Chem was previously (before v11.01) an offline CTM, driven by archived meteorological data at several static sets of global or regional 3-D grids,

with prescribed horizontal and vertical resolutions (Bey et al., 2001). Long et al. (2015) and Eastham et al. (2018) modularized the core processes in GEOS-Chem, including emissions, chemistry, convective mixing, planetary boundary layer mixing, and deposition processes, to work in modular units of 1-D atmospheric vertical columns. Information about the horizontal and

65 vertical grids, formerly fixed at compile-time, are now passed to the GEOS-Chem chemical module at run-time (Long et al., 2015; Eastham et al., 2018; Lin et al., 2020a). This modularization allows the same GEOS-Chem chemical code to be either driven by offline meteorological data (i.e., as a CTM) or be coupled online to dynamical models (Long et al., 2015; Eastham et al., 2018). To date, GEOS-Chem has been coupled to the NASA GEOS-5 earth system model (Hu et al., 2018), to the Beijing Climate Center atmospheric general circulation model (Lu et al., 2020), and to the WRF regional meteorological model (Lin

70 et al., 2020a) in distributed-memory frameworks for parallel computation. WRF-GC v2.0 is the first implementation of the GEOS-Chem model in an open-source dynamic model with chemical feedbacks to meteorology.

In this paper, we describe the development of WRF-GC v2.0, which includes the implementation of ARI, ACI, and the nested-domain capability. WRF-GC v2.0 allows GEOS-Chem users to investigate meteorology-atmospheric chemistry interactions at a wide range of resolutions. WRF-GC also offers other regional modellers access to the GEOS-Chem chemical core,

75 which is actively developed by a large user community and consistent with that in the GEOS-Chem offline CTM. WRF-GC v2.0 follows the modular coupling architecture of WRF-GC v1.0 (Section 2). In Section 3, we describe the representation of ARI and ACI in WRF-GC, which are implemented in the WRF-GC Coupler and abstracted from the parent models. In Section 4, we conduct a series of model experiments to evaluate the model performance at simulating meteorological fields and surface air pollutants over China, as well as to assess the impacts of ARI and ACI on regional meteorology and chemistry.

80 ## 2 Overview of the WRF-GC two-way coupled model architecture and its parent models

2.1 Architecture of the WRF-GC two-way coupled model

Figure 1 shows the architecture of the WRF-GC model, which consists of the two parent models (WRF and GEOS-Chem), and a WRF-GC coupler that is completely independent of both parent models. This architecture allows WRF-GC to use native, unmodified versions of the parent models, either one of which can be independently updated (Lin et al., 2020a). In

WRF-GC v1.0, the Coupler consists of a state conversion module, a state management module, and the GEOS-Chem column interface (Long et al., 2015; Eastham et al., 2018; Lin et al., 2020a). These modules manage the meteorological and chemical information in distributed memory and perform state conversions between the two models at runtime. A WRF-GC simulation is initialized by WRF, which sets the global clock, grids, and initial/boundary conditions. WRF performs dynamical and physical calculations, including the advection of chemical species, at each dynamical time step. At each chemical time step, the meteorological and chemical information is passed from WRF to GEOS-Chem through the WRF-GC Coupler. GEOS-Chem then performs convective mixing, dry deposition, emissions, planetary boundary-layer mixing, gas and aerosol chemistry, and wet scavenging, in this order (Lin et al., 2020a). Chemical information is then passed back to WRF for the next time step. At the end of the simulation, WRF finalizes the simulation and output the meteorological and chemical outcomes. In WRF-GC v1.0, the only chemistry-relevant operation performed by WRF is the grid-scale advection of chemical species; the chemical species do not otherwise interact with the WRF model.

In this work, we have implemented the ARI and the ACI into the two-way WRF-GC Coupler. Figure 1a shows the two-way WRF-GC Coupler, which extends the capabilities of the one-way Coupler by the addition of three modules: (1) the `Diag_Aero_Size_Info_Module`, (2) the `optical_driver`, and (3) the `mixactivate_driver`. These three modules diagnose the aerosol information from GEOS-Chem for the radiative transfer and cloud microphysics calculations in WRF. Figure 1b shows the workflow of the three new modules in WRF-GC v2.0. Users can switch on ARI or ACI by specifying `aer_ra_feedback=1` or `aer_cu_feedback=1`, respectively, in the WRF-GC configuration file (`namelist.input`). If ARI and ACI are both turned off, WRF-GC v2.0 will default to the one-way coupled simulation (Lin et al., 2020a).

When users turn on the ARI, ACI, or both, the three new modules are called by the WRF-to-Chemistry Interface (`chem_driver`) at the end of each chemical time step. The `Diag_Aero_Size_Info_Module` diagnoses the bulk aerosol mass information from GEOS-Chem (Section 2.2.1) and converts them into the sectional aerosol mass and number concentrations in specified size bins using prescribed size distributions (described in detail in Section 3.1). The sectional aerosol information is then used by the `optical_driver` (Section 3.3) and by the `mixactivate_driver` (Section 3.4) to calculate the aerosol and cloud optical properties and the activated cloud droplet number concentrations, respectively. The prognostic aerosol and

cloud information is then passed to the WRF model to be used by the radiative transfer (`module_radiation_driver`)

110 and cloud microphysics (`module_microphysics_driver`) calculations at the next time step.

The diagnostic variables of aerosol mass and number concentrations are added into the WRF-GC registry file (`registry.chem`). Users can specify which variables to output in the registry file. When WRF-GC is compiled, WRF will build all the output arrays based on the information in the registry file. Below we describe the details of the WRF and GEOS-Chem models pertinent to the two-way coupling. Further details on the two-way WRF-GC Coupler calculations are given in Section 3.

115 ## 2.2 Parent models

2.2.1 The GEOS-Chem model

WRF-GC v2.0 currently uses GEOS-Chem v12.7.2 (doi: 10.5281/zenodo.3701669) as its chemical module, but users can also subsequently update the chemical module to the latest standard version of GEOS-Chem through the existing WRF-GC architecture. The treatments for emissions, convective transport, boundary-layer mixing, gas and aerosol chemistry, dry deposition,

120 and wet scavenging of chemical species in GEOS-Chem v12.7.2 are mostly the same as those in GEOS-Chem v12.2.1, which is used in WRF-GC v1.0 and described in detail in Lin et al. (2020a). The standard chemical mechanism in GEOS-Chem v12.7.2 includes a comprehensive O_x-NO_x-VOC-halogen-aerosol chemical mechanism in the troposphere and uses the Unified tropospheric-stratospheric chemistry extension (UCX) for stratospheric chemistry (Eastham et al., 2014). One of the critical updates in GEOS-Chem v12.7.2 is that the sensitivity of surface resistance to temperature is reduced (Jaeglé et al., 2018). Also,

125 the bulk surface resistance of nitric acid is updated to $1 \, \mathrm{s \cdot cm^{-1}}$ to reflect its high affinity for natural surfaces. These updates increase the dry deposition velocities of the nitric acid and nitrate, thereby correcting the previous overestimation of surface nitrate concentrations, especially in winter (Jaeglé et al., 2018).

Aerosol species in the standard GEOS-Chem chemical mechanism include primary dust, sea salt, primary organic carbon aerosol (POC), primary black carbon aerosol (BC), secondary inorganic aerosols (sulfate, nitrate, ammonium), and secondary

130 organic aerosols (SOA) (Table 1). Sea salt aerosol masses in GEOS-Chem are simulated in two size ranges: the accumulation mode (dry radii between 0.1 and 0.5 μm) and the coarse mode (dry radii between 0.5 and 4 μm) (Jaeglé et al., 2011). Dust

aerosol masses are simulated in 4 size ranges, with effective radii of 0.7 μm, 1.4 μm, 2.4 μm, and 4.5 μm, respectively (Fairlie et al., 2007). All other aerosol species are simulated by their individual bulk masses, assuming static log-normal dry size distributions for each species (Martin et al., 2003; Drury et al., 2010; Jaeglé et al., 2011). Secondary inorganic aerosols are simulated with the ISORROPIA II algorithm (Fountoukis and Nenes, 2007). Freshly emitted POC and BC aerosols are assumed to be 50% hydrophobic and 50% hydrophilic, with a 1.2-day conversion timescale from hydrophobic to hydrophilic (Wang et al., 2014b). Primary organic aerosol masses are estimated from POC mass using either a default global organic aerosol to organic carbon (OA/OC) mass ratio of 2.1 or spatiotemporally-varying OA/OC ratios (Philip et al., 2014). GEOS-Chem model provides two options for simulating the formation of SOA. By default, GEOS-Chem uses the "simple SOA" scheme: biogenic isoprene and monoterpene, as well as CO emitted from anthropogenic and biomass burning activities, are taken as SOA precursors, which form SOA irreversibly at specified mass yields on a timescale of 1 day (Kim et al., 2015; Pai et al., 2020). This scheme simulates relatively accurate amounts of SOA without detailed chemical calculations (Miao et al., 2020). Alternatively, GEOS-Chem can calculate complex SOA formation based on the volatility basis set (VBS) scheme (Robinson et al., 2007; Pye et al., 2010). Oxidation of monoterpene and sesquiterpene form semivolatile products, while oxidation of light aromatics form intermediate volatility products (Pye et al., 2010). The complex SOA scheme also includes SOA formed via the aqueous-phase reactions of oxidation products from isoprene (Marais et al., 2016).

GEOS-Chem assumes static, log-normal dry size distributions for its simulated bulk aerosol species (except dust) for photolysis and heterogeneous chemistry calculations (Martin et al., 2003; Drury et al., 2010; Jaeglé et al., 2011). In addition, GEOS-Chem uses prescribed aerosol hygroscopicity and optical properties at multiple wavelengths under different relative humidity from the Global Aerosol Data Set (GADS) (Köpke et al., 1997; Martin et al., 2003) and updates from Latimer and Martin (2019) for photolysis and heterogeneous chemistry calculations.

In addition to the standard representation of aerosols described above, GEOS-Chem offers two optional schemes for sectional aerosol size-bin simulations: the Advanced Particle Microphysics (APM) (Yu and Luo, 2009) and the TwO-Moment Aerosol Sectional (TOMAS) microphysics packages (Kodros and Pierce, 2017). These options more accurately simulate size-dependent aerosol chemistry and microphysics, albeit at higher computational costs. However, these two size-resolved aerosol schemes are not yet supported by the WRF-GC Coupler.

In this work, we developed the two-way WRF-GC Coupler based on the standard bulk-mass representation of aerosol and the simple SOA scheme, involving the 10 aerosol species shown in Table 1. The goal is to include the ARI and ACI in WRF-GC while maintaining high computational efficiency. Our developed WRF-GC Coupler with ARI and ACI can be extended to the

160   APM and TOMAS schemes in the future, once those two schemes become compatible with the GEOS-Chem column interface.

2.2.2 The WRF model

WRF-GC v2.0 currently uses the WRF model (v3.9.1.1) to perform online calculations of meteorological processes, advection of chemical species, cloud microphysics, and radiative transfer with aerosol effects. WRF is a mesoscale numerical weather model for research and operational applications (Skamarock et al., 2008, 2019). WRF simulates atmospheric dynamics by

165   solving fully compressible, Eulerian non-hydrostatic equations on either hybrid sigma-eta (default) or terrain-following vertical coordinates. WRF uses the staggered Arakawa C-horizontal grids at resolutions of 100 km to 1 km and supports Lambert-conformal, Mercator, latitude-longitude, and polar stereographic projections. WRF offers multiple parameterization options for cloud microphysics, cumulus parameterization, planetary boundary layer physics, shortwave/longwave radiative transfer, and land surface physics (Skamarock et al., 2019). The options currently supported in WRF-GC are listed in Lin et al. (2020a).

170   To develop the ARI and ACI capabilities in WRF-GC v2.0, we use the radiative transfer and microphysics schemes in WRF that have been already coupled to the WRF-Chem model (Grell et al., 2005; Fast et al., 2006; Chapman et al., 2009), as described below.

In WRF, two shortwave radiation schemes have already been coupled to the prognostic aerosol information from WRF-Chem: the RRTMG shortwave radiation scheme (Iacono et al., 2008) and the Goddard shortwave radiation scheme (Chou

175   and Suarez, 1994). The RRTMG shortwave radiation scheme includes atmospheric Rayleigh scattering, molecular absorption by water vapor, ozone, oxygen, carbon dioxide, and methane, as well as the radiative extinction by clouds and aerosols in 14 spectral bands between 0.2 and 12.2 μm. The Goddard shortwave radiation scheme includes 11 spectral bands between 0.175 and 10 μm. It calculates atmospheric Rayleigh scattering, absorption by water vapor, ozone, oxygen, and carbon dioxide, as well as scattering and absorption by clouds and aerosols. For longwave radiation, only the RRTMG scheme (Iacono et al.,

180   2008) has been coupled to prognostic aerosol information. The RRTMG longwave radiation scheme accounts for the absorption

by water vapor, carbon dioxide, ozone, methane, oxygen, nitrous oxide, nitrogen, several halocarbons, as well as cloud and aerosols.

When ARI is turned on (`aer_ra_feedback=1` in `namelist.input`), the WRF model will ingest prognostic bulk aerosol optical information from the interface with the chemistry module. WRF further interpolates the aerosol optical proper-

185   ties to the specific wavelengths compatible with the shortwave radiation schemes. The AOD is interpolated or extrapolated using the Ångström exponent method (Eck et al., 1999), while the SSA and the asymmetry factor are linearly interpolated. If ARI is turned off (`aer_ra_feedback=0` in `namelist.input`), the RRTMG scheme ignores the aerosol effects on radiation (`aer_opt=0` in `namelist.input`), or uses climatological aerosol data from Tegen et al. (1997) (`aer_opt=1`), or uses the user-defined aerosol optical properties (`aer_opt=2`) specified in the WRF-GC configuration file (`namelist.input`).

190   For ACI, only two cloud microphysical schemes in the WRF model have been coupled to prognostic aerosol information: the Lin et al. scheme (Lin et al., 1983; Chen and Sun, 2002) and the Morrison two-moment scheme (Morrison et al., 2009). WRF uses an aerosol activation scheme developed by Abdul-Razzak and Ghan (2000, 2002). When ACI is turned on (`progn=1` and `naer=ignored` in `namelist.input`), the interface to the chemical module will call the aerosol activation scheme to diagnose the activated cloud droplet number in a time step. This calculation is based on a maximum supersaturation determined

195   by the mass concentrations, number densities, and hygroscopic properties of aerosols, as well as the local air temperature and updraft velocity. Also, the radiation module in WRF uses the prognostic liquid cloud effective radii to compute the liquid cloud optical depths (LCODs). If ACI is turned off, WRF either diagnoses the activated cloud droplet number using a prescribed aerosol number and size distribution (`progn=1` and `naer=specified`) or uses a constant source of activated cloud droplets ($100 \, \mathrm{cm^{-3}}$ per time step in the Lin et al. scheme and $250 \, \mathrm{cm^{-3}}$ per time step in the Morrison two-moment scheme) (`progn=0`).

200   Also, WRF uses constant values of liquid cloud effective radii to calculate LCODs if ACI is turned off. The Goddard shortwave radiation scheme assumes a constant effective radius of 10 μm for liquid cloud droplets. The RRTMG scheme assumes the effective radius of liquid cloud droplets to be 8 μm over land and 14 μm over the ocean.

3 New developments in WRF-GC v2.0

In Section 2, we describe the overall architecture of WRF-GC v2.0. Here, we describe the detailed diagnostics performed

205 in the two-way WRF-GC Coupler to communicate aerosol and cloud information between GEOS-Chem and WRF. Some of

our diagnostics are developed by imitating the connections between WRF and the chemical module in the WRF-Chem model

(Grell et al., 2005; Fast et al., 2006; Chapman et al., 2009). We also describe the software engineering developments that enable

nested-domain simulations in WRF-GC v2.0.

3.1 Diagnosing the size and number of dry aerosols

210 The size distribution of aerosol is a critical property that affects its optical effects and its ability to be activated into CCN. We

developed the (`Diag_Aero_Size_Info_Module`) to diagnose the sectional size distribution of aerosol mass and number

concentrations from the bulk aerosol masses simulated by GEOS-Chem. For each of the aerosol types (except dust) in GEOS-

Chem, we distribute the aerosol dry masses into 4 effective dry diameter bins used by WRF-GC. We assume the aerosol within

each size bin to be internally mixed. The lower and upper dry diameter bounds of the 4 bins (Table 2) are from the Model for

215 Simulating Aerosol Interactions and Chemistry (MOSAIC) 4-bins sectional parameterization (Zaveri et al., 2008). With the

exception of dust, we assumes that the number density of aerosol type i followed a log-normal distribution (Eq. 1):

$$n_i(\ln D_i) = \frac{dN}{d\ln D_i} = \frac{N}{\sqrt{2\pi}\ln\sigma_i}\exp[-\frac{(\ln D_i - \ln D_{g,i})^2}{2\ln^2\sigma_i}] \tag{1}$$

where D_i is the particle dry diameter, and N is the total number concentration of the internally-mixed particles. $n_i(\ln D_i)$ is

the number concentration density as a function of $\ln D_i$. $D_{g,i}$ and σ_i are the effective geometric mean dry diameter and the

220 effective geometric standard deviation of the log-normal distribution, respectively, which are prescribed for each aerosol type

(Table 1). Thus, the mass concentration density of the ith aerosol type ($m_i(\ln D_i)$) can be expressed using D_i, $n_i(\ln D_i)$, and

the density of aerosol type i (ρ_i), as shown in Eq. 2:

$$m_i(\ln D_i) = \rho_i \cdot \frac{\pi D_i^3}{6} \cdot n_i(\ln D_i) = \rho_i \cdot \frac{\pi D_i^3}{6} \cdot \frac{N}{\sqrt{2\pi} \ln \sigma_i} \exp[-\frac{(\ln D_i - \ln D_{g,i})^2}{2\ln^2 \sigma_i}] \qquad (2)$$

Table 1 summarizes the values of $D_{g,i}$, σ_i, and ρ_i for the aerosol types used in our two-way WRF-GC Coupler. The $D_{g,i}$ and

225   σ_i for secondary inorganic aerosols, BC, POC, and sea salt in accumulation and coarse modes are identical to the values used

in the GEOS-Chem model for photolysis and heterogeneous chemistry calculations (Martin et al., 2003; Drury et al., 2010;

Jaeglé et al., 2011). We assume that the log-normal distribution of SOA is identical to that of POC. The dry mass of aerosol

type i (except dust) in each of WRF-GC's 4 size bins can be calculated as Eq. 3:

$$M_{i,j} = M_i \cdot \frac{\int_{l_{W,j}}^{h_{W,j}} m_i(\ln D_i)\, d\ln D_i}{\int_0^\infty m_i(\ln D_i)\, d\ln D_i} \qquad (3)$$

230   where $l_{W,j}$ and $h_{W,j}$ are the lower and upper dry diameter bounds of the jth size bin. $M_{i,j}$ is the mass of aerosol type i in the

j^{th} bin, and M_i is the total mass of aerosol type i. The total number concentration of the internally-mixed aerosol population

(N) cancels out in Eq. 3.

GEOS-Chem simulates dust mass concentrations in 4 internal size bins, which need to be redistributed into the 4 size bins

used by WRF and WRF-GC (shown in Table 2). To achieve this, we mimicked the redistribution scheme of dust aerosols in

235   the Goddard Chemistry Aerosol Radiation Transport model (GOCART, Chin et al. (2002)), in which the first four internal size

bins are identical to those used in GEOS-Chem. In Eq. 4 and Eq. 5, the l and h with the subscripts W and G represent the

lower and upper dry diameter bounds of each size bin used in WRF-GC and GEOS-Chem, respectively. The indices j and k

refer to the size bins used by WRF-GC and GEOS-Chem, respectively ($j,k \in [1,4]$). Eq. 4 calculates the fraction of dust mass

within the GEOS-Chem size bin k that is mapped to the WRF-GC size bin j. The mass is distributed by the logarithmic of

240 particle diameter. $diag\_dst(j)$, the total dust mass concentrations within the WRF-GC size bin j, is the sum of the dust mass

mapped into that bin from the 4 GEOS-Chem dust size bins (Eq. 5).

$$dstfrac(j,k) = \frac{\max[\,0,\ \min[\ln h_W(j), \ln h_G(k)] - \max[\ln l_W(j), \ln l_G(k)]\,]}{\ln h_G(k) - \ln l_G(k)} \tag{4}$$

$$diag\_dst(j) = \sum_{k=1}^{4} dst(k) \cdot dstfrac(j,k) \quad j,k \in [1,4] \tag{5}$$

Eq. 6 diagnoses the number concentrations of the internally-mixed aerosols in each size bin. The total dry aerosol volume

245 in the jth size bin ($\sum_{i=1}^{10} V_{d,i,j}$) is calculated by summing the dry aerosol volume of the 10 aerosol types. The aerosol number

concentrations in j^{th} size bin, N_j, can then be diagnosed by dividing the total dry aerosol volume in that size bin by the mean

particle size (Eq. 6).

$$N_j = \frac{6}{\pi \left[\frac{1}{2}(l_W(j) + h_W(j))\right]^3} \cdot \sum_{i=1}^{10} V_{d,i,j} \tag{6}$$

3.2 Diagnosing water uptake of aerosols

250 The hygroscopic growth of aerosols at ambient relative humidity impacts their wet radii and optical properties. We follow the

method developed by Petters and Kreidenweis (2007, 2013) to diagnose the uptake of water by aerosols and the resulting wet

radii. According to the Zandovskii, Stoles, and Robinson (ZSR) assumption (Stokes and Robinson, 1966), the total aerosol

liquid water is equal to the sum of the water uptaken by each aerosol constituent, as shown in Eq. 7:

$$V_{w,j} = \frac{a_w}{1-a_w} \sum_{i=1}^{10} \kappa_i V_{d,i,j} \tag{7}$$

255 where $V_{w,j}$ is the total volume of aerosol liquid water in the size bin j. a_w is the water activity, equal to the fractional relative

humidity. κ_i is the hygroscopicity of the aerosol type i (Table 1). The wet radii of the internal-mixed aerosols in the jth size

bin, $R_{w,j}$, are required for the calculation of aerosol optical properties and are calculated by Eq. 8:

$$R_{w,j} = \frac{1}{2} \left(\frac{6}{\pi} \cdot \frac{V_{w,j} + \sum_{i=1}^{10} V_{d,i,j}}{N_j} \right)^{\frac{1}{3}} \tag{8}$$

3.3 Aerosol-radiation interactions

260 When ARI is turned on in WRF-GC v2.0, the new `optical_driver` module calls the `module_optical_averaging`

to diagnose the bulk optical properties of the internally-mixed aerosols at each model grid and pass them to WRF for radiative

transfer calculations. The diagnosed bulk optical properties include the AOD, the SSA, and the asymmetry factor at 4 specific

wavelengths (300, 400, 600, 999 nm) for shortwave radiative transfer, and the AOD at 16 specific wavelengths for longwave

radiative transfer. Our `module_optical_averaging` is developed by modifying a similar module from WRF-Chem

265 (Fast et al., 2006). The `module_optical_averaging` module ingests the wet radii ($R_{w,j}$) and the number concentrations

(N_j) of aerosol particles in the jth size bin. The bulk refractive indices for the internally-mixed aerosols in each size bin are

calculated by volume-weighting the refractive indices for individual aerosol species using a look-up table (Barnard et al., 2010).

The tabulated refractive indices for water, sulfate, dust, sea salt, and primary and secondary OC are wavelength-dependent,

while the refractive indices for other aerosol species do not vary with wavelength. The module then uses the bulk refractive

270 indices to calculate the bulk extinction efficiency (Q_e), the bulk scattering efficiency (Q_s), and the intermediate asymmetry

factor (g') for the internally-mixed aerosols as a function of the size parameter α_j ($= \frac{2\pi R_{w,j}}{\lambda}$) based on Mie theory (Wiscombe, 1979). We use a Chebyshev economization (Press et al., 1992) to avoid the full Mie calculation at each time step following Fast et al. (2006). A full Mie calculation is only performed at the first chemical time step to obtain the Chebyshev expansion coefficients for each complex refractive indices.

275   The bulk total extinction coefficient (b_{ext}) at wavelength λ is calculated as the sum of extinction by aerosols in all 4 size bins (Eq. 9):

$$b_{ext}(\lambda) = \sum_{j=1}^{4} Q_e(\alpha_j) \cdot \pi R_{w,j}^2 \cdot N_j \tag{9}$$

The bulk AOD in a layer of atmosphere of dz thickness is (Eq. 10):

$$\tau(\lambda) = b_{ext}(\lambda) \cdot dz \tag{10}$$

280   The single scattering albedo (ϖ_0), which represents the scattered percentage in the total light extinction of aerosol particles, is calculated as (Eq. 11):

$$\varpi_0(\lambda) = \frac{b_s(\lambda)}{b_{ext}(\lambda)} \tag{11}$$

where b_s is the scattering coefficient of aerosols, given by (Eq. 12):

$$b_s(\lambda) = \sum_{j=1}^{4} Q_s(\alpha_j) \cdot \pi R_{w,j}^2 \cdot N_j \tag{12}$$

285   The bulk asymmetry factor, g, represents the asymmetry between the forward scattering and backward scattering of aerosol

particles:

$$g(\lambda) = \frac{\sum\limits_{j=1}^{4} Q_s(\alpha_j) \cdot \pi R_{w,j}^2 \cdot N_j \cdot g'(\alpha_j)}{b_s(\lambda)} \tag{13}$$

where g' is the intermediate asymmetry factor related to the size parameter α_j.

3.4   Aerosol-cloud interactions

290   We couple the activation of aerosol particles to the Morrison two-moment scheme (Morrison et al., 2009) and the Lin et al.

scheme (Lin et al., 1983; Chen and Sun, 2002) in WRF-GC. To achieve this, we develop an interface routine `wrfgc_mixactivate`

(contained in `module_mixactivate_wrappers` in the Coupler) by mimicking a similar routine in WRF-Chem. Eq. 14

shows the rate of change of the cloud droplet number concentration (N_c) within a WRF model grid in the two cloud micro-

physical schemes. The rate of change of N_c is determined by the advection of cloud droplet number ($-\mathbf{V} \bullet \nabla N_c$), the vertical

295   transport of cloud droplet number (D), the loss rate of cloud droplet number due to collision, coalescence, and collection (C),

the evaporation of cloud droplets (E), as well as the rate of cloud droplet activation (S).

$$\frac{\partial N_c}{\partial t} = -(\mathbf{V} \bullet \nabla N_c) + D - C - E + S \tag{14}$$

When ACI is turned on (`aer_cu_feedback=1` and `progn=1`) in WRF-GC, the `mixactivate_driver` module in

the WRF-GC Coupler calls the existing WRF subroutine `mixactivate` through an interface routine (`wrfgc_mixactivate`)

300   to calculate the number of aerosol particles activated into cloud droplets (S) and pass it to WRF. `wrfgc_mixactivate` first

calculates the volume-weighted bulk hygroscopocity using the diagnostic aerosol mass and number within each aerosol size

bin and then calls the subroutine `mixactivate`. The subroutine `mixactivate` uses the Köhler theory to calculate the acti-

vated aerosol mass and number when the ambient supersaturation is over the critical supersaturation of aerosols (Abdul-Razzak

and Ghan, 2000, 2002). The total aerosol mass and number concentrations are treated as two explicit population: interstitial

305 and cloud-borne. The prognostic aerosol mass and number concentrations are initialized as interstitial before passing to the

`mixactivate_driver` module. The activated aerosols will be then considered cloud-borne, while the unactivated aerosols

remain interstitial. The `mixactivate` subroutine also calculates CCN at six specified supersaturation ratios (0.02%, 0.05%,

0.1%, 0.2%, 0.5%, and 1%) as output diagnostics.

3.5 Development of nested-grid functionality and online lightning NO$_x$ emissions

310 We implement the nested-domain functionality into WRF-GC v2.0 to enable meteorology-chemistry simulations at higher

resolution. In WRF-GC v1.0 (Lin et al., 2020a), the coupling between WRF and GEOS-Chem was limited to a single domain

of arbitrary dimension and resolution; the nesting of multiple model domains was not supported. This was because the modules

in the GEOS-Chem model (prior to v12.4.0) used a single memory space for the entire simulation, such that the domain

dimensions in GEOS-Chem were fixed once the simulation was initialized.

315 We improve the State Management Module in WRF-GC v2.0 to better control the memory space of GEOS-Chem. Figure 2

illustrates the operation of the state management module when running WRF-GC v2.0 in a nested-domain configuration. When

running a nested-domain simulation, WRF designates separate memory space for each domain, and at each time step WRF

alternately accesses the memory spaces for each domain. To achieve the same functionality in GEOS-Chem, we modify the

GEOS-Chem model (implemented in the standard code for v12.4.0 and after) so that all of its internal variables are saved into

320 state objects (meteorology, chemistry, and diagnostic state variables), which are labeled for the specific simulation domain. We

then modify the State Management Module, such that at each time step during run-time, the State Management Module will

determine the GEOS-Chem domain being processed, access the corresponding state objects, and provide them to GEOS-Chem.

In addition, the emission module of GEOS-Chem, HEMCO, is recently updated (Keller et al., 2014; Lin et al., 2020b), such

that its memory space is also fully objectified. This allows WRF-GC v2.0 to execute separate copies of HEMCO for each of

325 the nested domains.

WRF-GC v2.0 also supports both one-way and two-way information exchange between the nested domains, as provided

by the WRF framework. In a nested-domain simulation, the outer (coarser) domain will always provide lateral boundary

conditions to its immediate inner (finer) domain (one-way information exchange). In addition, users can turn on two-way

information exchange option (`feedback=1` in the WRF-GC namelist), which further allows information from the inner

330   domain be averaged and fed back to to the immediate outer domain at every time step.

In addition to the existing meteorology-dependent emissions, we further implement online lightning NO_x emissions in

WRF-GC v2.0 by coupling WRF meteorology to the lightning NO_x emission scheme in the HEMCO module. Intra-cloud and

cloud-to-ground flash densities are functions of the cloud-top height and are calculated by the lightning parameterization in

WRF (Price and Rind, 1992; Wong et al., 2013). HEMCO then calculates lightning NO_x emissions using the prescribed NO_x

335   production rates (500 moles per flash for latitudes northward of 35°N; 260 moles per flash elsewhere) (Murray et al., 2012)

and vertically distributed them from the surface to the local convective cloud top level (Ott et al., 2010).

4   Validation of WRF-GC simulations of regional meteorology and surface pollutant concentrations over China

4.1   Setup of model experiments

We conduct two control simulations with full aerosol-cloud-radiation interactions using WRF-GC v2.0, one during January

340   2015 (Case Winter) and one during July 2016 (Case Summer), to evaluate the model's performance in simulating surface

$PM_{2.5}$ and ozone concentrations, AOD, and cloud optical properties. Table 3 summarizes the setup of our simulations. Figure

3c shows our simulation domain, set by a Mercator projection at 27 km × 27 km spatial resolution. The simulations are

discretized vertically at 50 layers, extending from the surface to 10 hPa. The Case Winter simulation was for January 4 to

29, 2015. The Case Summer simulation was for June 27 to July 31, 2016. The first four days of each simulation initialize the

345   model. Meteorological IC/BCs are taken from the NCEP FNL dataset (doi:10.5065/D6M043C6) at 1° resolution. Chemical

IC/BCs are from a GEOS-Chem global simulation at 2.5° longitude × 2° latitude, interpolated to WRF-GC horizontal and

vertical grids. Both meteorological and chemical BCs are updated every 6 hours in WRF-GC.

We further design four sensitivity simulations over China for July 2016 with different combinations of ARI and ACI to

investigate the impacts of chemical feedbacks on simulated meteorology and air quality. The setup of these four sensitivity

350   simulations is identical to that of Case Summer, except ARI and ACI are configured differently in each of the sensitivity

simulations (Table 3). In Case ACR, both ARI and ACI are turned on; this is identical to the Case Summer control simulation. In Case NO_ACR, both ARI and ACI are turned off, i.e., identical to a one-way WRF-GC simulation with no chemical feedbacks to meteorology. The Case ARI and Case ACI sensitivity simulations include either only ARI or only ACI, respectively.

Chinese monthly mean anthropogenic emissions are from the Multi-resolution Emission Inventory for China (MEIC; Li et al. (2014)), which include emissions from power generation, industry, transportation, residential activities, and agriculture sectors at a resolution of $0.25°$ for the years 2015 and 2016. Anthropogenic emissions from the rest of Asia are from Li et al. (2017a), developed for the year 2010. Monthly mean biomass burning emissions are from the Global Emissions Database version 4 (GFED4; Randerson et al. (2018)). Biogenic emissions are calculated online using the Model of Emissions of Gases and Aerosols from Nature (MEGAN; Guenther et al. (2012)), implemented in the HEMCO module (Keller et al., 2014) in GEOS-Chem. Other meteorology-dependent emissions, including the emissions of sea salt (Gong, 2003), dust (Zender et al., 2003), soil NO_x (Hudman et al., 2012), and lightning NO_x (Murray et al., 2012), are also calculated online in the HEMCO module.

4.2 Observation datasets

4.2.1 Satellite retrievals of AOD, cloud optical properties and surface downward shortwave radiation

We use satellite observations to evaluate WRF-GC's performance in simulating aerosol and cloud optical properties. Monthly mean AOD observations are from the Deep Blue Level-3 monthly and daily aerosol products (AERDB_D3/M3_VIIRS_SNPP, version 1) from the Visible Infrared Imaging Radiometer Suite (VIIRS) instruments at a spatial resolution of $1°$ (Sayer et al., 2018). Briefly, VIIRS is on board the Suomi National Polar-orbiting Partnership (SNPP) satellite, launched in 2011 with an Equator-overpassing time at 13:30 local time. VIIRS records data in 22 spectral bands at visible and thermal infrared wavebands. The monthly gridded products aggregate the 6-minute Level 2 swath data. Missing values of monthly mean AOD may be due to the obstruction by clouds, high reflectance by snow and ice, or sun glint. Monthly liquid cloud optical depth (LCOD) observations are from the VIIRS/SNPP Cloud Properties Level-3 monthly $1°$ grid products (CLDPROP_D3/M3_VIIRS_SNPP, version 1.1) (Platnick et al., 2019). LCOD is retrieved from the non-absorbing visible, near-infrared or shortwave infrared

channels of VIIRS using the bi-spectral solar reflectance algorithm (Nakajima et al., 1991). The Level-3 gridded products are

375 also derived from the 6-minute Level-2 data.

We validate the surface downward shortwave radiation simulated by WRF-GC using the latest Earth Polychromatic Imaging Camera (EPIC)-derived products over land at $0.1°$ spatial resolution (Hao et al. (2020), https://doi.org/10.25584/1595069). The EPIC instrument is on-board the Deep Space Climate Observatory (DSCOVR) satellite, launched in February 2015 to the Sun-Earth first Lagrange point (Burt and Smith, 2012). EPIC observes the sunlit part of the Earth at 10 spectral bands

380 from the ultraviolet to near-infrared wavelengths every 1 to 2 hours; thus it is able to estimate the global downward shortwave radiation with high spatiotemporal resolution. The EPIC-derived total downward shortwave radiation is consistent with the ground-based observations with a low global bias of -0.71 Wm^{-2} over land. The spatiotemporal variations in the EPIC-derived surface downward shortwave radiation agrees well with the Clouds and the Earth's Radiant Energy System Synoptic (CERES) data (Hao et al., 2020).

385 4.2.2 AOD from Aerosol Robotic Network (AERONET) project

We evaluate the spectral AOD simulated by WRF-GC against the ground-based observations from the Aerosol Robotic Network (AERONET). AERONET observes aerosol optical properties using the CIMEL Electronique multiband sun photometer https://aeronet.gsfc.nasa.gov/). Holben et al. (1998) showed that the uncertainty of AERONET AOD under cloud-free condition was less than ± 0.01 for wavelengths over than 440 nm. We use the Version 3, Level 2.0 quality-assured dataset (Giles

390 et al., 2019), where the cloud-contaminated points and instrumental anomalies are removed. We select four representative sites in Eastern China, where there are more than 50 % of valid observations of spectral AOD at three wavelengths (500 nm, 675 nm, and 1020 nm) during January 2015. These four sites are: (1) Chinese Academy of Meteorological Sciences (CAMS) in Beijing (116.32°E, 39.93°N), (2) Xianghe (116.96°E, 39.75°N), (3) China University of Mining and Technology in Xuzhou (117.14°E, 34.22°N), and (4) Hong Kong Polytechnic University in Hong Kong (114.18°E, 22.30°N). At each site, We calcu-

395 late the daily mean of observed spectral AOD at each of the three wavelengths (500 nm, 675 nm, and 1020 nm) in January 2015.

4.2.3 Surface measurements of air pollutants and temperature

Hourly surface measurements of $PM_{2.5}$ and ozone are managed by the Ministry of Ecology and Environment (MEE) of China (www.cnemc.cn). Our protocol for data quality control follows Jiang et al. (2020). We remove sites with less than 90 % valid

400 hourly data during January 2015 and July 2016. In model grids containing multiple sites, we select the site closest to the center of the WRF-GC grid. In all, we compare model results to summertime ozone observations at 581 sites and wintertime $PM_{2.5}$ at 512 sites, respectively. Surface air temperature measurements at 371 sites over China are from the U.S. National Climate Data Center (https://gis.ncdc.noaa.gov/maps/ncei/cdo/hourly). We remove the sites with less than 90 % valid data during July 2016. We use the surface measurements at 215 sites to evaluate the simulated surface air temperature in July 2016.

405 ### 4.3 Validation of the simulated AOD over East Asia

Figure 3a and 3c compare the AOD at 550 nm wavelength over East Asia as observed by VIIRS and as simulated by WRF-GC (Case Winter) during January 8 to 28 2015. For comparison against VIIRS observations, we use the simulated AODs at 300 nm and 999 nm to calculate the Ångström exponent of the internally-mixed bulk aerosol and then scale the AOD at 400 nm to obtain the simulated AOD at 550 nm. WRF-GC is generally able to reproduce the spatial distribution of AOD observed

410 by VIIRS over Eastern China (105°E to 130°E, 20°N to 40°N) with a spatial correlation coefficient of r = 0.64. WRF-GC reproduces the high AOD values over the Sichuan Basin but underestimates the AOD over other parts of Eastern China. The observed and simulated AODs over Eastern China are 0.37 and 0.21, respectively. WRF-GC also underestimates the AOD over Xinjiang Province, likely reflecting an underestimation of dust.

Figure 3b and 3d compare the observed and simulated (Case Summer) mean AOD at 550 nmin July 2016. VIIRS observes

415 AOD values exceeding 0.6 over the NCP area, reflecting the large amounts of aerosols and their hygroscopic growth over that area. The simulated spatial distribution of AOD is generally consistent with that from VIIRS, but the peak values are lower than the observations by 50% over the NCP. We also compare model results to the AOD observations from the MODIS instrument (Platnick et al., 2017) and similarly find that the simulated AODs are spatially consistent but lower than the MODIS observations over Eastern China.

420   Figure 4 compares the time series of the simulated daily spectral AOD against the AERONET observations at the four

representative Chinese sites (Beijing, Xianghe, Xuzhou, and Hong Kong) during January 8 to 28 2015. At each site, we

compare the simulated spectral AODs at 550 nm, 600 nm, and 999 nm to the observed spectral AODs at wavelengths 500 nm,

675 nm, and 1020 nm, respectively. WRF-GC reproduces the observed day-to-day variation of AOD at these four sites during

January 2015. The temporal correlation coefficients between the observed and simulated AODs at all sites and wavelengths

425   range between 0.55 and 0.87 (significant at 5 % significance level), except for the correlation coefficient between the observed

and simulated AOD at 550 nm in Beijing (0.44). However, the simulated AODs are consistently lower than the AERONET

AODs, especially during high AOD events.

Our analyses above show that AODs simulated by WRF-GC reproduce the spatiotemporal variability of the AODs observed

by satellite and ground-based networks. However, the simulated AOD are consistently lower than these observations. Previous

430   comparisons of AODs simulated by regional models against satellite observations often found spatial consistency but significant

low biases in the model (Gao et al., 2014; Gan et al., 2015; Xing et al., 2015; Zhang et al., 2016). The reasons for this are

yet unclear (Curci et al., 2015). The WRF-GC model may have underestimated the abundance of aerosols in the regional

atmosphere, as indicated by the slight underestimation of surface $PM_{2.5}$ concentrations shown below (Figure 9). It is also

possible that the model's internal mixing assumption leads to a large uncertainty of the AODs (Fassi-Fihri et al., 1997; Curci

435   et al., 2015). Several studies showed that the regional distributions of AOD observed by VIIRS and MODIS were consistent

with the AERONET measurements. However, both VIIRS and MODIS observations were generally biased-high compared to

AERONET observations over Asia (Wang et al., 2020). This high-bias in the satellite-observed AOD may partially account for

the discrepancy between the simulated and satellite AODs.

4.4   Validation of the simulated LCOD and liquid cloud droplet effective radii

440   Figure 5a and 5b compare the July mean LCODs retrieved by VIIRS and those from the Case Summer (identical to Case

ACR) simulation in July 2016. The spatial distributions of observed and simulated LCOD are generally consistent, with higher

LCOD over land than over the ocean. Over land, the observed and simulated LCODs are both high over Northeastern China,

over central-western China, and along the southern slopes of the Himalayas. In contrast, the observed and simulated LCODs

are relatively low over the Tibetan Plateau. The simulated domain-average LCOD from Case Summer is 11.8 ± 8.5, in good

445 agreement with the domain-averaged LCOD retrieved by VIIRS (18.4 ± 7.2). The underestimation of simulated LCOD is

mostly over the South China Sea and the Tibetan Plateau. Over Eastern China, the simulated magnitude and spatiotemporal

patterns of LCOD are in good agreement with the observations (spatial correlation coefficient r = 0.61, normalized mean bias

= -19.6%).

Figure 6 shows the monthly mean liquid cloud effective radii at cloud top from the Case Summer simulation (i.e., the Case

450 ACR simulation). Satellite retrievals of cloud effective radii often show large biases, except over areas dominated by liquid

stratocumulus or stratus (Yan et al., 2015; Witte et al., 2018). We instead compare the simulated liquid cloud effective radii to

the reported values from aircraft observations over China. The observed effective radii of liquid cloud droplets over the NCP

area in summer are in the range of 5.1 μm (± 2.2 μm) to 6.3 μm (± 2.3 μm) (Deng et al., 2009; Zhang et al., 2011b; Zhao et al.,

2018). Over Southern China, the observed effective radii of liquid cloud droplets in summer vary from 7.3 ± 1.7 μm to 7.9

455 ± 3.0 μm (Hao et al., 2017; Yang et al., 2020). Our simulated effective radii of liquid cloud droplets are consistent with these

observed sizes of liquid cloud droplets and reflect the spatial difference between Northern and Southern China. The simulated

mean effective radii are 8.4 ± 1.3 μm and 10.7 ± 0.9 μm over the NCP and Southern China in July 2016, respectively.

4.5 Validation of simulated surface downward shortwave radiation and surface air temperature over China

Figure 7a and 7b compare the July mean surface downward shortwave radiation (SWDOWN) over East Asia from the EPIC-

460 derived data and those from the Case Summer simulation in 2016. The simulated spatial distribution of July mean SWDOWN

is in good agreement with that observed by EPIC over China, with a spatial correlation coefficient r = 0.73. The simulated

monthly mean SWDOWN exceeded 300 $\mathrm{Wm^{-2}}$ over the Tibetan Plateau and Northwestern China but are approximately 200

$\mathrm{Wm^{-2}}$ over Southeastern China. The observed and simulated July mean SWDOWN over China are 288.1 $\mathrm{Wm^{-2}}$ (± 36.1

$\mathrm{Wm^{-2}}$) and 272.4 $\mathrm{Wm^{-2}}$ (± 47.6 $\mathrm{Wm^{-2}}$), respectively, with a slight low bias of -5.4% in the model.

465 Figure 8a shows the good agreement between the simulated surface air temperature (Case Summer simulation) and the

surface measurements over China in July 2016. The spatial correlation coefficient between the observed and simulated surface

air temperature is 0.92, with a small model NMB of -3.7%. Our validations above demonstrate the capability of two-way coupled WRF-GC in reproducing the regional meteorology.

4.6 Validation of simulated surface concentrations of PM$_{2.5}$ and ozone over China

470 We next assess WRF-GC's performance in simulating surface air pollutant concentrations over China in January 2015 and July 2016. Figure 9a shows the observed and simulated (Case Winter) PM$_{2.5}$ concentrations during January 8 to January 28 2015. WRF-GC reproduces the observed spatial distributions of PM$_{2.5}$ over Eastern China (eastward of 108°E) in January 2015; the spatial correlation between the observed and simulated PM$_{2.5}$ concentrations is 0.74. WRF-GC successfully captures the high PM$_{2.5}$ in Central China and over the Sichuan Basin, but the model underestimates the PM$^{2.5}$ concentrations in the North China

475 Plain (NCP) and Northwestern China. The simulated mean PM$_{2.5}$ concentration over Eastern China (87.5 ± 37.2 µgm^{-3}) is 6.6% lower than the observations (93.7 ± 33 µgm^{-3}).

Figure 9b compares the observed and simulated (Case Summer) afternoon (13:00 to 17:00 local sun time) surface ozone concentrations over China during July 2016. The simulated afternoon ozone concentrations are in good agreement with the surface measurements over China. The spatial correlation coefficient between the observed and simulated July surface ozone

480 concentrations is 0.56 over Eastern China. The average observed and simulated ozone concentrations over Eastern China are 54 ± 13 ppbv and 64 ± 17 ppbv, respectively. The normalized mean bias of the simulation is 19%. The overestimation of surface ozone concentrations is mostly in the Henan and Shanxi Provinces over the NCP. Our analysis demonstrates WRF-GC's general capability in reproducing the spatial patterns of Chinese surface PM$_{2.5}$ and ozone in winter and in summer, respectively, particularly over the heavily polluted Eastern China.

485 ## 5 Impacts of ARI and ACI on simulated meteorology and surface ozone concentration in China in summer

5.1 Impacts of the ARI and ACI on summertime meteorology

We examine the individual and combined impacts of ARI and ACI on the simulated monthly mean LCOD, surface downward shortwave radiation, and surface air temperature in July 2016, respectively. Figure 5d shows the impacts of ARI and ACI on

the simulated LCOD in July 2016. Without ARI and ACI, the model severely overestimates the VIIRS-observed LCOD over

490   East Asia, particularly over Central China, around Japan and Korea, and along the southern slopes of the Himalayas (Figure

5c). By turning on both ARI and ACI, the simulated July mean LCOD decrease significantly over these areas and are in

better agreement with the VIIRS observations. We further find that these improvements are mainly due to the inclusion of ACI

(Figure 5e and 5f). By turning on the ACI, the simulated cloud water content and the simulated liquid cloud effective radii both

decrease relative to those in the NO_ACR simulation.

495   The shortwave extinction by aerosol and clouds affect the transfer of shortwave radiation to the surface. Figure 7d compares

the simulated July mean SWDOWN from the cases ACR and NO_ACR. The combined impacts of ARI and ACI lead to

increased simulated SWDOWN by 20 to 50 W m^{-2} over Southwestern China and the Yangtze River Delta (YRD) area, while

reducing the simulated SWDOWN by 10 to 50 W m^{-2} over the NCP, the Sichuan Basin and the Bohai Sea. Including both

ARI and ACI improves the spatial correlation coefficients from 0.57 (Case NO_ACR) to 0.73 (Case ACR) over China. We

500   found that these changes mostly reflect the impacts of ACI (Figure 7f). The exceptions are over the NCP and Northeastern

China, where the high values of AOD lead to a significant decrease in the simulated SWDOWN (Figure 3d and Figure 7e)

when ARI is turned on.

The ARI and ACI also significantly affect the simulated surface air temperature. Figure 8c compares the simulated July

mean surface air temperature from the cases ACR and NO_ACR. The combined impact of ARI and ACI lead to higher surface

505   temperatures over Northeastern China, the YRD area, and around the Gulf of Bohai. In contrast, ARI and ACI combine to

reduce the simulated surface air temperature over Central China. Figure 8b shows the overestimation of surface air temperature

over Central China when the ARI and ACI are both turned off. Our sensitivity simulations indicate that these simulated changes

are due to complex and spatially-varied responses to either ARI or ACI (Figure 8d and 8e). In addition, the simulated responses

of surface air temperature to ARI and ACI are not always consistent with the simulated responses of SWDOWN. For example,

510   over the Tibetan Plateau, the combination of ARI and ACI drives large increases in surface downward solar radiation but do

not lead to much higher surface air temperature. This may be because the inclusion of ACI reduced the simulated LCOD over

the Tibetan Plateau, which may have increased the downward shortwave radiation while decreasing the downward longwave

radiation, thus partially neutralizing the changes in radiative fluxes.

5.2 Impacts of ARI and ACI on summertime afternoon surface ozone concentrations over China

515 Figure 10 shows the combined and individual effects of the ARI and ACI on the simulated monthly mean surface afternoon

ozone concentrations in July 2016, relative to the Case NO_ACR experiment. By turning on both ARI and ACI, the July mean

afternoon surface ozone concentrations significantly decrease by 2 to 10 ppbv over Henan Province and the Sichuan Basin.

Over the YRD area and Eastern Inner Mongolia, however, turning on ARI and ACI leads to increases of afternoon surface

ozone concentrations by up to 10 ppbv. These varied responses are due to the spatially-varied responses of surface ozone to

520 ARI and ACI, respectively, which are not additive. For example, ARI lead to increased surface air temperature over the YRD

area, while both ARI and ACI lead to increased SWDOWN over that area. These meteorological responses lead to enhanced

local biogenic VOC emissions and increased surface ozone. Over the Eastern Inner Mongolia area, ACI lead to increased

surface temperature and shortwave radiation, which significantly enhances the surface ozone concentration. Over the Beijing-

Tianjin-Hebei (BTH) area of China, where summertime ozone pollution is most severe (Lu et al., 2018), the impacts of ARI

525 and ACI are complex. Their combined effect is to increase surface ozone in the northern parts while decreasing surface ozone

in the southern parts.

We compare the simulated monthly mean afternoon ozone concentrations from Case ACR and Case NO_ACR against the

surface ozone measurements in China and over three megacities. Figure 11 shows the scatter plots of the observed and simulated

monthly mean surface afternoon ozone concentrations over China (581 sites), in the BTH area (32 sites), in the Pearl River

530 Delta (PRD) area (20 sites), and in the YRD area (32 sites) during July 2016. The simulated monthly mean afternoon ozone

concentrations from Case ACR and Case NO_ACR are 22 % and 28 % higher than the observations over China, respectively.

The improvement in simulated surface ozone due to the overall effects of the ARI and ACI is more evident over the three

megacities. Including both ARI and ACI in WRF-GC leads to smaller biases in the statistics between simulated and observed

surface ozone concentrations in all three megacities. The slopes of simulated versus observed ozone concentrations improve

535 from 1.58 to 1.39 in the BTH and from 1.43 to 1.24 in the PRD. The slope of simulated versus observed ozone concentrations

in the YRD do not change, but the intercept is reduced from -7.3 ppbv to -2.5 ppbv.

6 Conclusions

We present here version 2.0 of the WRF-GC model, an online two-way coupling of the WRF meteorological model and the GEOS-Chem chemical model with aerosol-radiation interactions and aerosol-cloud interactions, as well as the nested-domain

540   capability. The coupling structure of WRF-GC v2.0 is abstracted and modular, which allows the two parent models to be updated independently and stay state-of-the-science. The chemical module from GEOS-Chem is benchmarked, well-documented, evaluated, and actively developed by research groups worldwide. New developments in GEOS-Chem can be easily incorporated into WRF-GC under its modular architecture. In addition, all WRF-GC v2.0 features can be parallelized using MPI, which allow the model to scale to massively-parallel architectures. WRF-GC v2.0 enables GEOS-Chem users to investigate

545   the interactions between meteorology and atmospheric chemistry for any region at a wide range of spatial resolutions. At the same time, WRF-GC offers other regional modellers access to the GEOS-Chem chemical core.

We implement the ARI and ACI into WRF-GC v2.0 by adding three modules with the following functions: (1) diagnosing the size and number of the bulk aerosols simulated by GEOS-Chem, (2) computing aerosol optical properties, and (3) computing the number of aerosol particles activated into cloud droplets. The aerosol optical properties and cloud droplet number source

550   are then passed to the WRF model for radiative transfer and cloud microphysics calculations. We develop WRF-GC'se nested-domain capability by improving the state management module and the memory-management in GEOS-Chem (implemented as of GEOS-Chem version 12.4.0). The nested-domain capability enables WRF-GC simulations at higher spatial resolution simulations while being computationally efficient.

Our test simulations show that the WRF-GC model with the full aerosol-cloud-radiation interactions is able to reproduce the

555   spatial distributions of wintertime $PM_{2.5}$ and summertime ozone with small biases compared with the surface measurements. WRF-GC v2.0 generally reproduces the spatial distributions of monthly mean AOD compared with the satellite-based retrievals by VIIRS. The day-to-day variation of AOD is in good agreement with the ground-based observations from AERONET over four sites in eastern China during January 2015. Coupling the cloud droplet activation to aerosol masses simulated by GEOS-Chem improves the simulated July mean liquid cloud optical depth and liquid cloud effective radii to better agree with VIIRS

560   and aircraft observations. In China and in three Chinese megacities currently experiencing severe surface ozone pollution

(BTH, PRD, and YRD), the inclusion of ARI and ACI also leads to improved simulated surface ozone concentrations, relative to the simulation without ARI and ACI.

WRF-GC (v2.0) is the first coupling of GEOS-Chem to an open-source meteorological model with chemical feedbacks. The modules developed for WRF-GC v2.0 can also facilitate future two-way couplings between GEOS-Chem and other dynamical models. Supports for the size-resolved aerosol schemes (APM and TOMAS) in WRF-GC are currently under development, which will better represent aerosol microphysics. We envision WRF-GC to become a powerful tool for research, forecast, and regulatory applications of regional atmospheric chemistry and air quality.

Code availability.

WRF-GC is free and open-source and can be obtained at http://wrf.geos-chem.org. The current version of WRF-GC (v2.0) described in this paper supports WRF v3.9.1.1 and GEOS-Chem v12.7.2 and is permanently archived at https://github.com/jimmielin/wrf-gc-pt2-paper-code (last accessed: December 19, 2020) (DOI: 10.5281/zenodo.4362624). The nested-grid functionality of WRF-GC described in this paper is permanently archived at https://github.com/jimmielin/wrf-gc-pt2-paper-code-nested (last accessed: December 27, 2020) (DOI: 10.5281/zenodo.4395258). The two parent models, WRF and GEOS-Chem, are also open-source and can be obtained from their developers at https://www.mmm.ucar.edu/weather-research-and-forecasting-model (last accessed: December 19, 2020) and http://www.geos-chem.org (last accessed: December 19, 2020), respectively.

Author contributions.

TMF envisioned and oversaw the project. XF designed the two-way WRF-GC Coupler. HL developed the nested-grid functionality in WRF-GC. MPS, JZ and DJJ assisted in the adaptation of the GEOS-Chem FlexGrid functionality to WRF-GC. XF and HL developed the WRF-GC code, with assistance from HT, YM, LZ and XW. XF performed the simulations and analysis. XF, HL, and TMF wrote the manuscript. All authors contributed to the manuscript.

Competing interests. The authors declare no competing interests.

Acknowledgements. This work was supported by the National Natural Science Foundation of China (41975158, 42011530176) and the Shenzhen Science and Technology Innovation Committee (KCXFZ202002011008038). Computational resources were provided by the Center for Computational Science and Engineering at the Southern University of Science and Technology. Work at Harvard was supported by
585 the NASA Atmospheric Composition Modeling and Analysis Program.

References

Abdul-Razzak, H. and Ghan, S.: A parameterization of aerosol activation 2. Multiple aerosol types, J. Geophys. Res. Atmos., 105, 6837–6844, https://doi.org/10.1029/1999JD901161, 2000.

Abdul-Razzak, H. and Ghan, S.: A parameterization of aerosol activation 3. Sectional representation, J. Geophys. Res. Atmos., 107, https://doi.org/10.1029/2001JD000483, 2002.

Abel, D., Holloway, T., Kladar, R. M., Meier, P., Ahl, D., Harkey, M., and Patz, J.: Response of Power Plant Emissions to Ambient Temperature in the Eastern United States, Environ. Sci. Technol., 51, 5838–5846, https://doi.org/10.1021/acs.est.6b06201, 2017.

Archer-Nicholls, S., Lowe, D., Schultz, D. M., and McFiggans, G.: Aerosol-radiation-cloud interactions in a regional coupled model: the effects of convective parameterisation and resolution, Atmos. Chem. Phys., 16, 5573–5594, https://doi.org/10.5194/acp-16-5573-2016, 2016.

Baklanov, A., Schluenzen, K., Suppan, P., Baldasano, J., Brunner, D., Aksoyoglu, S., Carmichael, G., Douros, J., Flemming, J., Forkel, R., Galmarini, S., Gauss, M., Grell, G., Hirtl, M., Joffre, S., Jorba, O., Kaas, E., Kaasik, M., Kallos, G., Kong, X., Korsholm, U., Kurganskiy, A., Kushta, J., Lohmann, U., Mahura, A., Manders-Groot, A., Maurizi, A., Moussiopoulos, N., Rao, S. T., Savage, N., Seigneur, C., Sokhi, R. S., Solazzo, E., Solomos, S., Sorensen, B., Tsegas, G., Vignati, E., Vogel, B., and Zhang, Y.: Online coupled regional meteorology chemistry models in Europe: current status and prospects, Atmos. Chem. Phys., 14, 317–398, https://doi.org/10.5194/acp-14-317-2014, 2014.

Barnard, J. C., Fast, J. D., Paredes-Miranda, G., Arnott, W. P., and Laskin, A.: Technical Note: Evaluation of the WRF-Chem "Aerosol Chemical to Aerosol Optical Properties" Module using data from the MILAGRO campaign, Atmos. Chem. Phys., 10, 7325–7340, https://doi.org/10.5194/acp-10-7325-2010, 2010.

Bey, I., Jacob, D. J., Yantosca, R. M., Logan, J. A., Field, B. D., Fiore, A. M., Li, Q., Liu, H. Y., Mickley, L. J., and Schultz, M. G.: Global modeling of tropospheric chemistry with assimilated meteorology: Model description and evaluation, J. Geophys. Res. Atmos., 106, 23 073–23 095, https://doi.org/10.1029/2001JD000807, 2001.

Burt, J. and Smith, B.: Deep space climate observatory: The DSCOVR mission, 2012 IEEE Aerospace Conference, Big Sky, MT, USA, 3–10 March 2012, 2012.

Byun, D. and Schere, K. L.: Review of the governing equations, computational algorithms, and other components of the Models-3 Community Multiscale Air Quality (CMAQ) modeling system, Appl. Mech. Rev., 59, 51–77, https://doi.org/10.1115/1.2128636, 2006.

Chapman, E. G., Gustafson Jr., W. I., Easter, R. C., Barnard, J. C., Ghan, S. J., Pekour, M. S., and Fast, J. D.: Coupling aerosol-cloud-radiative processes in the WRF-Chem model: Investigating the radiative impact of elevated point sources, Atmos. Chem. Phys., 9, 945–964, https://doi.org/10.5194/acp-9-945-2009, 2009.

Chen, F. and Dudhia, J.: Coupling an advanced land surface-hydrology model with the Penn State-NCAR MM5 modeling system. Part I: Model implementation and sensitivity, Mon. Weather Rev., 129, 569–585, https://doi.org/10.1175/1520-0493(2001)129<0569:CAALSH>2.0.CO;2, 2001a.

Chen, F. and Dudhia, J.: Coupling an advanced land surface-hydrology model with the Penn State-NCAR MM5 modeling system. Part II: Preliminary model validation, Mon. Weather Rev., 129, 587–604, https://doi.org/10.1175/1520-0493(2001)129<0587:CAALSH>2.0.CO;2, 2001b.

Chen, S. and Sun, W.: A One-dimensional Time Dependent Cloud Model, J. Meteorol. Soc. Jap. Ser. II, 80, 99–118, https://doi.org/10.2151/jmsj.80.99, 2002.

Chin, M., Ginoux, P., Kinne, S., Torres, O., Holben, B., Duncan, B., Martin, R., Logan, J., Higurashi, A., and Nakajima, T.: Tropospheric aerosol optical thickness from the GOCART model and comparisons with satellite and Sun photometer measurements, J. Atmos. Sci., 59, 461–483, https://doi.org/10.1175/1520-0469(2002)059<0461:TAOTFT>2.0.CO;2, 2002.

Chou, M. D. and Suarez, M. J.: An efficient thermal infrared radiation parameterization for use in general circulation models, NASA Tech. Memo., 104506, 3, 85pp, 1994.

Curci, G., Hogrefe, C., Bianconi, R., Im, U., Balzarini, A., Baró, R., Brunner, D., Forkel, R., Giordano, L., Hirtl, M., Honzak, L., Jiménez-Guerrero, P., Knote, C., Langer, M., Makar, P., Pirovano, G., Pérez, J., San José, R., Syrakov, D., Tuccella, P., Werhahn, J., Wolke, R., Žabkar, R., Zhang, J., and Galmarini, S.: Uncertainties of simulated aerosol optical properties induced by assumptions on aerosol physical and chemical properties: An AQMEII-2 perspective, Atmos. Environ., 115, 541 – 552, https://doi.org/10.1016/j.atmosenv.2014.09.009, 2015.

Deng, Z., Zhao, C., Zhang, Q., Huang, M., and Ma, X.: Statistical analysis of microphysical properties and the parameterization of effective radius of warm clouds in Beijing area, Atmos. Res., 93, 888–896, https://doi.org/10.1016/j.atmosres.2009.04.011, 2009.

Ding, A. J., Fu, C. B., Yang, X. Q., Sun, J. N., Petäjä, T., Kerminen, V.-M., Wang, T., Xie, Y., Herrmann, E., Zheng, L. F., Nie, W., Liu, Q., Wei, X. L., and Kulmala, M.: Intense atmospheric pollution modifies weather: a case of mixed biomass burning with fossil fuel combustion pollution in eastern China, Atmos. Chem. Phys., 13, 10 545–10 554, https://doi.org/10.5194/acp-13-10545-2013, 2013.

Drury, E., Jacob, D. J., Spurr, R. J. D., Wang, J., Shinozuka, Y., Anderson, B. E., Clarke, A. D., Dibb, J., McNaughton, C., and Weber, R.: Synthesis of satellite (MODIS), aircraft (ICARTT), and surface (IMPROVE, EPA-AQS, AERONET) aerosol observations over eastern North America to improve MODIS aerosol retrievals and constrain surface aerosol concentrations and sources, J. Geophys. Res. Atmos., 115, https://doi.org/10.1029/2009JD012629, 2010.

Eastham, S. D., Weisenstein, D. K., and Barrett, S. R.: Development and evaluation of the unified tropospheric–stratospheric chemistry extension (UCX) for the global chemistry-transport model GEOS-Chem, Atmos. Environ., 89, 52–63, https://doi.org/10.1016/j.atmosenv.2014.02.001, 2014.

Eastham, S. D., Long, M. S., Keller, C. A., Lundgren, E., Yantosca, R. M., Zhuang, J., Li, C., Lee, C. J., Yannetti, M., Auer, B. M., Clune, T. L., Kouatchou, J., Putman, W. M., Thompson, M. A., Trayanov, A. L., Molod, A. M., Martin, R. V., and Jacob, D. J.: GEOS-Chem High Performance (GCHP v11-02c): a next-generation implementation of the GEOS-Chem chemical transport model for massively parallel applications, Geosci. Model. Dev., 11, 2941–2953, https://doi.org/10.5194/gmd-11-2941-2018, 2018.

Eck, T., Holben, B., Reid, J., Dubovik, O., Smirnov, A., O'Neill, N., Slutsker, I., and Kinne, S.: Wavelength dependence of the optical depth of biomass burning, urban, and desert dust aerosols, J. Geophys. Res. Atmos., 104, 31 333–31 349, https://doi.org/10.1029/1999JD900923, 1999.

Fairlie, T. D., Jacob, D. J., and Park, R. J.: The impact of transpacific transport of mineral dust in the United States, Atmos. Environ., 41, 1251–1266, https://doi.org/10.1016/j.atmosenv.2006.09.048, 2007.

Fassi-Fihri, A., Suhre, K., and Rosset, R.: Internal and external mixing in atmospheric aerosols by coagulation: Impact on the optical and hygroscopic properties of the sulphate-soot system, Atmos. Environ., 31, 1393 – 1402, https://doi.org/10.1016/S1352-2310(96)00341-X, 1997.

Fast, J. D., Gustafson Jr., W. I., Easter, R. C., Zaveri, R. A., Barnard, J. C., Chapman, E. G., Grell, G. A., and Peckham, S. E.: Evolution of ozone, particulates, and aerosol direct radiative forcing in the vicinity of Houston using a fully coupled meteorology-chemistry-aerosol model, J. Geophys. Res. Atmos., 111, https://doi.org/10.1029/2005JD006721, 2006.

660   Flemming, J., Inness, A., Flentje, H., Huijnen, V., Moinat, P., Schultz, M. G., and Stein, O.: Coupling global chemistry transport models to
      ECMWF's integrated forecast system, Geosci. Model. Dev., 2, 253–265, https://doi.org/10.5194/gmd-2-253-2009, 2009.

      Forkel, R., Werhahn, J., Hansen, A. B., McKeen, S., Peckham, S., Grell, G., and Suppan, P.: Effect of aerosol-radiation feedback on regional
      air quality - A case study with WRF/Chem, Atmos. Environ., 53, 202–211, https://doi.org/10.1016/j.atmosenv.2011.10.009, 2012.

      Fountoukis, C. and Nenes, A.: ISORROPIA II: a computationally efficient thermodynamic equilibrium model for K^+- Ca^{2+}- Mg^{2+}- NH_4^+-
665   Na^+- SO_4^{2-}- NO_3^-- Cl^-- H_2O aerosols, Atmos. Chem. Phys., 7, 4639–4659, https://doi.org/10.5194/acp-7-4639-2007, 2007.

      Gan, C. M., Pleim, J., Mathur, R., Hogrefe, C., Long, C. N., Xing, J., Wong, D., Gilliam, R., and Wei, C.: Assessment of long-term
      WRF–CMAQ simulations for understanding direct aerosol effects on radiation "brightening" in the United States, Atmos. Chem. Phys.,
      15, 12 193–12 209, https://doi.org/10.5194/acp-15-12193-2015, 2015.

      Gao, Y., Zhao, C., Liu, X., Zhang, M., and Leung, L. R.: WRF-Chem simulations of aerosols and anthropogenic aerosol radiative forcing in
670   East Asia, Atmos. Environ., 92, 250–266, https://doi.org/10.1016/j.atmosenv.2014.04.038, 2014.

      Giles, D. M., Sinyuk, A., Sorokin, M. G., Schafer, J. S., Smirnov, A., Slutsker, I., Eck, T. F., Holben, B. N., Lewis, J. R., Campbell, J. R.,
      Welton, E. J., Korkin, S. V., and Lyapustin, A. I.: Advancements in the Aerosol Robotic Network (AERONET) Version 3 database
      – automated near-real-time quality control algorithm with improved cloud screening for Sun photometer aerosol optical depth (AOD)
      measurements, Atmos. Meas. Tech., 12, 169–209, https://doi.org/10.5194/amt-12-169-2019, 2019.

675   Gong, S. L.: A parameterization of sea-salt aerosol source function for sub-and super-micron particles, Global Biogeochem. Cy., 17,
      https://doi.org/10.1029/2003GB002079, 2003.

      Gong, W., Makar, P. A., Zhang, J., Milbrandt, J., Gravel, S., Hayden, K. L., Macdonald, A. M., and Leaitch, W. R.: Modelling aerosol-
      cloud-meteorology interaction: A case study with a fully coupled air quality model (GEM-MACH), Atmos. Environ., 115, 695–715,
      https://doi.org/10.1016/j.atmosenv.2015.05.062, 2015.

680   Grell, G. A., Peckham, S. E., Schmitz, R., McKeen, S. A., Frost, G., Skamarock, W. C., and Eder, B.: Fully coupled "online" chemistry
      within the WRF model, Atmos. Environ., 39, 6957–6975, https://doi.org/10.1016/j.atmosenv.2005.04.027, 2005.

      Guenther, A. B., Jiang, X., Heald, C. L., Sakulyanontvittaya, T., Duhl, T., Emmons, L. K., and Wang, X.: The Model of Emissions of Gases
      and Aerosols from Nature version 2.1 (MEGAN2.1): an extended and upYeard framework for modeling biogenic emissions, Geosci.
      Model. Dev., 5, 1471–1492, https://doi.org/10.5194/gmd-5-1471-2012, 2012.

685   Hansen, J., Sato, M., and Ruedy, R.: Radiative forcing and climate response, J. Geophys. Res., 102, 6831–6864,
      https://doi.org/10.1029/96JD03436, 1997.

      Hao, D., Asrar, G. R., Zeng, Y., Zhu, Q., Wen, J., Xiao, Q., and Chen, M.: DSCOVR/EPIC-derived global hourly and daily down-
      ward shortwave and photosynthetically active radiation data at $0.1° \times 0.1°$ resolution, Earth Syst. Sci. Data, 12, 2209–2221,
      https://doi.org/10.5194/essd-12-2209-2020, 2020.

690   Hao, J., Yin, Y., Kuang, X., Chen, J., Yuan, L., Xiao, H., Li, Z., Pu, M., Wang, J., Zhou, X., Chen, Y., and Wu, Y.: Aircraft Mea-
      surements of the Aerosol Spatial Distribution and Relation with Clouds over Eastern China, Aerosol Air. Qual. Res., 17, 3230–3243,
      https://doi.org/10.4209/aaqr.2016.12.0576, 2017.

      Haywood, J. and Boucher, O.: Estimates of the direct and indirect radiative forcing due to tropospheric aerosols: A review, Rev. Geophys.,
      38, 513–543, https://doi.org/10.1029/1999RG000078, 2000.

695   Holben, B., Eck, T., Slutsker, I., Tanre, D., Buis, J., Setzer, A., Vermote, E., Reagan, J., Kaufman, Y., Nakajima, T., Lavenu, F., Jankowiak,
      I., and Smirnov, A.: AERONET - A federated instrument network and data archive for aerosol characterization, Remote Sens. Environ.,
      66, 1–16, https://doi.org/10.1016/S0034-4257(98)00031-5, 1998.

Hong, S.-Y., Noh, Y., and Dudhia, J.: A New Vertical Diffusion Package with an Explicit Treatment of Entrainment Processes, Mon. Weather Rev., 134, 2318–2341, https://doi.org/10.1175/MWR3199.1, 2006.

700 Hu, L., Keller, C. A., Long, M. S., Sherwen, T., Auer, B., Da Silva, A., Nielsen, J. E., Pawson, S., Thompson, M. A., Trayanov, A. L., Travis, K. R., Grange, S. K., Evans, M. J., and Jacob, D. J.: Global simulation of tropospheric chemistry at 12.5 km resolution: performance and evaluation of the GEOS-Chem chemical module (v10-1) within the NASA GEOS Earth system model (GEOS-5 ESM), Geosci. Model Dev., 11, 4603–4620, https://doi.org/10.5194/gmd-11-4603-2018, 2018.

Huang, X., Ding, A., Liu, L., Liu, Q., Ding, K., Niu, X., Nie, W., Xu, Z., Chi, X., Wang, M., Sun, J., Guo, W., and Fu, C.: Effects of
705 aerosol-radiation interaction on precipitation during biomass-burning season in East China, Atmos. Chem. Phys., 16, 10 063–10 082, https://doi.org/10.5194/acp-16-10063-2016, 2016.

Hudman, R. C., Moore, N. E., Mebust, A. K., Martin, R. V., Russell, A. R., Valin, L. C., and Cohen, R. C.: Steps towards a mechanistic model of global soil nitric oxide emissions: implementation and space based-constraints, Atmos. Chem. Phys., 12, 7779–7795, https://doi.org/10.5194/acp-12-7779-2012, 2012.

710 Iacono, M. J., Delamere, J. S., Mlawer, E. J., Shephard, M. W., Clough, S. A., and Collins, W. D.: Radiative forcing by long-lived greenhouse gases: Calculations with the AER radiative transfer models, J. Geophys. Res. Atmos., 113, https://doi.org/10.1029/2008JD009944, 2008.

Jaeglé, L., Quinn, P. K., Bates, T. S., Alexander, B., and Lin, J.-T.: Global distribution of sea salt aerosols: new constraints from in situ and remote sensing observations, Atmos. Chem. Phys., 11, 3137–3157, https://doi.org/10.5194/acp-11-3137-2011, 2011.

Jaeglé, L., Shah, V., Thornton, J. A., Lopez-Hilfiker, F. D., Lee, B. H., McDuffie, E. E., Fibiger, D., Brown, S. S., Veres, P., Sparks, T. L.,
715 Ebben, C. J., Wooldridge, P. J., Kenagy, H. S., Cohen, R. C., Weinheimer, A. J., Campos, T. L., Montzka, D. D., Digangi, J. P., Wolfe, G. M., Hanisco, T., Schroder, J. C., Campuzano-Jost, P., Day, D. A., Jimenez, J. L., Sullivan, A. P., Guo, H., and Weber, R. J.: Nitrogen Oxides Emissions, Chemistry, Deposition, and Export Over the Northeast United States During the WINTER Aircraft Campaign, J. Geophys. Res. Atmos., 123, 12 368–12 393, https://doi.org/10.1029/2018JD029133, 2018.

Jiang, Z., Jolleys, M. D., Fu, T.-M., Palmer, P. I., Ma, Y. P., Tian, H., Li, J., and Yang, X.: Spatiotemporal and probability variations of surface
720 PM2.5 over China between 2013 and 2019 and the associated changes in health risks: An integrative observation and model analysis, Sci. Total. Environ., 723, 137 896, https://doi.org/10.1016/j.scitotenv.2020.137896, 2020.

Jimenez, P. A., Dudhia, J., Gonzalez-Rouco, J. F., Navarro, J., Montavez, J. P., and Garcia-Bustamante, E.: A Revised Scheme for the WRF Surface Layer Formulation, Mon. Weather Rev., 140, 898–918, https://doi.org/10.1175/MWR-D-11-00056.1, 2012.

Johnson, B., Shine, K., and Forster, P.: The semi-direct aerosol effect: Impact of absorbing aerosols on marine stratocumulus, Q. J. Roy.
725 Meteor. Soc., 130, 1407–1422, https://doi.org/10.1256/qj.03.61, 2004.

Kaminski, J. W., Neary, L., Struzewska, J., McConnell, J. C., Lupu, A., Jarosz, J., Toyota, K., Gong, S. L., Côté, J., Liu, X., Chance, K., and Richter, A.: GEM-AQ, an on-line global multiscale chemical weather modelling system: model description and evaluation of gas phase chemistry processes, Atmos. Chem. Phys., 8, 3255–3281, https://doi.org/10.5194/acp-8-3255-2008, 2008.

Keller, C. A., Long, M. S., Yantosca, R. M., Da Silva, A. M., Pawson, S., and Jacob, D. J.: HEMCO v1.0: a versatile, ESMF-compliant
730 component for calculating emissions in atmospheric models, Geosci. Model Dev., 7, 1409–1417, https://doi.org/10.5194/gmd-7-1409-2014, 2014.

Kim, P. S., Jacob, D. J., Fisher, J. A., Travis, K., Yu, K., Zhu, L., Yantosca, R. M., Sulprizio, M. P., Jimenez, J. L., Campuzano-Jost, P., Froyd, K. D., Liao, J., Hair, J. W., Fenn, M. A., Butler, C. F., Wagner, N. L., Gordon, T. D., Welti, A., Wennberg, P. O., Crounse, J. D., St. Clair, J. M., Teng, A. P., Millet, D. B., Schwarz, J. P., Markovic, M. Z., and Perring, A. E.: Sources, seasonality, and trends of southeast

735   US aerosol: an integrated analysis of surface, aircraft, and satellite observations with the GEOS-Chem chemical transport model, Atmos. Chem. Phys., 15, 10 411–10 433, https://doi.org/10.5194/acp-15-10411-2015, 2015.

Kodros, J. and Pierce, J.: Important global and regional differences in aerosol cloud-albedo effect estimates between simulations with and without prognostic aerosol microphysics, J. Geophys. Res. Atmos., 122, 4003–4018, https://doi.org/10.1002/2016JD025886, 2017.

Köpke, P., Hess, M., Schult, I., and Shettle, E. P.: Global aerosol data set, report, Max-Planck Inst. für Meteorol., Hamburg, Germany,, 1997.

740   Latimer, R. N. C. and Martin, R. V.: Interpretation of measured aerosol mass scattering efficiency over North America using a chemical transport model, Atmos. Chem. Phys., 19, 2635–2653, https://doi.org/10.5194/acp-19-2635-2019, 2019.

Li, M., Zhang, Q., Streets, D. G., He, K. B., Cheng, Y. F., Emmons, L. K., Huo, H., Kang, S. C., Lu, Z., Shao, M., Su, H., Yu, X., and Zhang, Y.: Mapping Asian anthropogenic emissions of non-methane volatile organic compounds to multiple chemical mechanisms, Atmos. Chem. Phys., 14, 5617–5638, https://doi.org/10.5194/acp-14-5617-2014, 2014.

745   Li, M., Zhang, Q., Kurokawa, J.-i., Woo, J.-H., He, K., Lu, Z., Ohara, T., Song, Y., Streets, D. G., Carmichael, G. R., Cheng, Y., Hong, C., Huo, H., Jiang, X., Kang, S., Liu, F., Su, H., and Zheng, B.: MIX: a mosaic Asian anthropogenic emission inventory under the international collaboration framework of the MICS-Asia and HTAP, Atmos. Chem. Phys., 17, 935–963, https://doi.org/10.5194/acp-17-935-2017, 2017a.

Li, Z., Xia, X., Cribb, M., Mi, W., Holben, B., Wang, P., Chen, H., Tsay, S.-C., Eck, T. F., Zhao, F., Dutton, E. G., and Dickerson, R. R.:
750   Aerosol optical properties and their radiative effects in northern China, J. Geophys. Res., 112, https://doi.org/10.1029/2006JD007382, 2007.

Li, Z., Guo, J., Ding, A., Liao, H., Liu, J., Sun, Y., Wang, T., Xue, H., Zhang, H., and Zhu, B.: Aerosol and boundary-layer interactions and impact on air quality, Natl. Sci. Rev., 4, 810–833, https://doi.org/10.1093/nsr/nwx117, 2017b.

Lin, H., Feng, X., Fu, T.-M., Tian, H., Ma, Y., Zhang, L., Jacob, D. J., Yantosca, R. M., Sulprizio, M. P., Lundgren, E. W., Zhuang, J., Zhang,
755   Q., Lu, X., Zhang, L., Shen, L., Guo, J., Eastham, S. D., and Keller, C. A.: WRF-GC (v1.0): online coupling of WRF (v3.9.1.1) and GEOS-Chem (v12.2.1) for regional atmospheric chemistry modeling – Part 1: Description of the one-way model, Geosci. Model Dev., 13, 3241–3265, https://doi.org/10.5194/gmd-13-3241-2020, 2020a.

Lin, H., Jacob, D. J., Lundgren, E. W., Sulprizio, M. P., Keller, C. A., Fritz, T. M., Eastham, S. D., Goldhaber, S., Emmons, L. K., Campbell, P. C., Baker, B., and Montuoro, R.: Development of the Harmonized Emissions Component (HEMCO) 3.0 as a general emissions
760   component for atmospheric models, AGU 2020 Fall Meeting, A022-04, 2020b.

Lin, Y. L., Farley, R. D., and Orville, H. D.: Bulk Parameterization of The Snow Field in A Cloud Model, Journal of Climate and Applied Meteorology, 22, 1065–1092, https://doi.org/10.1175/1520-0450(1983)022<1065:BPOTSF>2.0.CO;2, 1983.

Lohmann, U. and Feichter, J.: Global indirect aerosol effects: a review, Atmos. Chem. Phys., 5, 715–737, https://doi.org/10.5194/acp-5-715-2005, 2005.

765   Long, M. S., Yantosca, R., Nielsen, J. E., Keller, C. A., da Silva, A., Sulprizio, M. P., Pawson, S., and Jacob, D. J.: Development of a grid-independent GEOS-Chem chemical transport model (v9-02) as an atmospheric chemistry module for Earth system models, Geosci. Model Dev., 8, 595–602, https://doi.org/10.5194/gmd-8-595-2015, 2015.

Lu, X., Hong, J., Zhang, L., Cooper, O. R., Schultz, M. G., Xu, X., Wang, T., Gao, M., Zhao, Y., and Zhang, Y.: Severe Surface Ozone Pollution in China: A Global Perspective, Environ. Sci. Technol. Lett., 5, 487–494, https://doi.org/10.1021/acs.estlett.8b00366, 2018.

770   Lu, X., Zhang, L., Wu, T., Long, M. S., Wang, J., Jacob, D. J., Zhang, F., Zhang, J., Eastham, S. D., Hu, L., Zhu, L., Liu, X., and Wei, M.: Development of the global atmospheric chemistry general circulation model BCC-GEOS-Chem v1.0: model description and evaluation, Geosci. Model Dev., 13, 3817–3838, https://doi.org/10.5194/gmd-13-3817-2020, 2020.

Ma, Y., Fu, T. M., Tian, H., Gao, J., Hu, M., Guo, J., Zhang, Y., Sun, Y., Zhang, L., Yang, X., and Wang, X.: Emergency Response Measures to Alleviate a Severe Haze Pollution Event in Northern China during December 2015: Assessment of Effectiveness, Aerosol Air Qual.
775   Res., 20, https://doi.org/10.4209/aaqr.2019.09.0442, 2020.

Marais, E. A., Jacob, D. J., Jimenez, J. L., Campuzano-Jost, P., Day, D. A., Hu, W., Krechmer, J., Zhu, L., Kim, P. S., Miller, C. C., Fisher, J. A., Travis, K., Yu, K., Hanisco, T. F., Wolfe, G. M., Arkinson, H. L., Pye, H. O. T., Froyd, K. D., Liao, J., and McNeill, V. F.: Aqueous-phase mechanism for secondary organic aerosol formation from isoprene: application to the southeast United States and co-benefit of SO2 emission controls, Atmos. Chem. Phys., 16, 1603–1618, https://doi.org/10.5194/acp-16-1603-2016, 2016.

780   Martin, R. V., Jacob, D. J., Yantosca, R. M., Chin, M., and Ginoux, P.: Global and regional decreases in tropospheric oxidants from photo-chemical effects of aerosols, J. Geophys. Res. Atmos., 108, 4097, https://doi.org/10.1029/2002JD002622, 2003.

Miao, R., Chen, Q., Zheng, Y., Cheng, X., Sun, Y., Palmer, P. I., Shrivastava, M., Guo, J., Zhang, Q., Liu, Y., Tan, Z., Ma, X., Chen, S., Zeng, L., Lu, K., and Zhang, Y.: Model bias in simulating major chemical components of PM$_{2.5}$ in China, Atmos. Chem. Phys., 20, 12 265–12 284, https://doi.org/10.5194/acp-20-12265-2020, 2020.

785   Morrison, H., Thompson, G., and Tatarskii, V.: Impact of Cloud Microphysics on the Development of Trailing Stratiform Precipitation in a Simulated Squall Line: Comparison of One- and Two-Moment Schemes, Mon. Weather Rev., 137, 991–1007, https://doi.org/10.1175/2008MWR2556.1, 2009.

Murray, L. T., Jacob, D. J., Logan, J. A., Hudman, R. C., and Koshak, W. J.: Optimized regional and interannual variabil-ity of lightning in a global chemical transport model constrained by LIS/OTD satellite data, J. Geophys. Res. Atmos., 117,
790   https://doi.org/10.1029/2012JD017934, 2012.

Nakajima, T., King, M. D., Spinhirne, J. D., and Radke, L. F.: Determination of the Optical Thickness and Effective Particle Radius of Clouds from Reflected Solar Radiation Measurements. Part I: Theory, Nature, 517, 41.e1–41.e21, 1991.

Ott, L. E., Pickering, K. E., Stenchikov, G. L., Allen, D. J., DeCaria, A. J., Ridley, B., Lin, R.-F., Lang, S., and Tao, W.-K.: Production of lightning NOx and its vertical distribution calculated from three-dimensional cloud-scale chemical transport model simulations, J.
795   Geophys. Res. Atmos., 115, https://doi.org/10.1029/2009JD011880, 2010.

Pai, S. J., Heald, C. L., Pierce, J. R., Farina, S. C., Marais, E. A., Jimenez, J. L., Campuzano-Jost, P., Nault, B. A., Middlebrook, A. M., Coe, H., Shilling, J. E., Bahreini, R., Dingle, J. H., and Vu, K.: An evaluation of global organic aerosol schemes using airborne observations, Atmos. Chem. Phys., 20, 2637–2665, https://doi.org/10.5194/acp-20-2637-2020, 2020.

Petaja, T., Jarvi, L., Kerminen, V. M., Ding, A. J., Sun, J. N., Nie, W., Kujansuu, J., Virkkula, A., Yang, X. Q., Fu, C. B., Zilitinkevich, S.,
800   and Kulmala, M.: Enhanced air pollution via aerosol-boundary layer feedback in China, Sci. Rep., 6, https://doi.org/10.1038/srep18998, 2016.

Petters, M. D. and Kreidenweis, S. M.: A single parameter representation of hygroscopic growth and cloud condensation nucleus activity, Atmos. Chem. Phys., 7, 1961–1971, https://doi.org/10.5194/acp-7-1961-2007, 2007.

Petters, M. D. and Kreidenweis, S. M.: A single parameter representation of hygroscopic growth and cloud condensation nucleus activity -
805   Part 3: Including surfactant partitioning, Atmos. Chem. Phys., 13, 1081–1091, https://doi.org/10.5194/acp-13-1081-2013, 2013.

Philip, S., Martin, R. V., Pierce, J. R., Jimenez, J. L., Zhang, Q., Canagaratna, M. R., Spracklen, D. V., Nowlan, C. R., Lamsal, L. N., Cooper, M. J., and Krotkov, N. A.: Spatially and seasonally resolved estimate of the ratio of organic mass to organic carbon, Atmos. Environ., 87, 34–40, https://doi.org/10.1016/j.atmosenv.2013.11.065, 2014.

Platnick, S., King, M., and Hubanks, P.: MODIS Atmosphere L3 Monthly Product. NASA MODIS Adaptive Processing System, God-
dard Space Flight Center, USA, http://dx.doi.org/10.5067/MODIS/MOD08_M3.061;http://dx.doi.org/10.5067/MODIS/MYD08_M3.061,
2017.

Platnick, S., Meyer, K. G., Hubanks, P., Holz, R., Ackerman, S. A., and Heidinger, A. K.: VIIRS Atmosphere L3 Cloud Properties Product.
Version-1.1. NASA Level-1 and Atmosphere Archive and Distribution System (LAADS) Distributed Active Archive Center (DAAC),
Goddard Space Flight Center, USA, http://dx.doi.org/10.5067/VIIRS/CLDPROP_M3_VIIRS_SNPP.011, 2019.

Press, W. H., Teukolsky, S. A., and Flannery, B. P.: Numerical Recipes., Cambridge Univ. Press, New York, 1992.

Price, C. and Rind, D.: A Simple Lightning Parameterization for Calculating Global Lightning Distributions, J. Geophys. Res. Atmos., 97,
9919–9933, https://doi.org/10.1029/92JD00719, 1992.

Pye, H. O. T., Chan, A. W. H., Barkley, M. P., and Seinfeld, J. H.: Global modeling of organic aerosol: the importance of reactive nitrogen
(NO_x and NO_3), Atmos. Chem. Phys., 10, 11 261–11 276, https://doi.org/10.5194/acp-10-11261-2010, 2010.

Randerson, J., G.R., v. d. W., L., G., G.J., C., and P.S., K.: Global Fire Emissions Database, Version 4, (GFEDv4). ORNL DAAC, Oak Ridge,
Tennessee, USA., https://doi.org/10.3334/ORNLDAAC/1293, 2018.

Renner, E. and Wolke, R.: Modelling the formation and atmospheric transport of secondary inorganic aerosols with special attention to
regions with high ammonia emissions, Atmos. Environ., 44, 1904 – 1912, https://doi.org/10.1016/j.atmosenv.2010.02.018, 2010.

Robinson, A. L., Donahue, N. M., Shrivastava, M. K., Weitkamp, E. A., Sage, A. M., Grieshop, A. P., Lane, T. E., Pierce,
J. R., and Pandis, S. N.: Rethinking organic aerosols: Semivolatile emissions and photochemical aging, Science, 315, 1259–1262,
https://doi.org/10.1126/science.1133061, 2007.

Sayer, A. M., Hsu, N. C., Lee, J., Bettenhausen, C., Kim, W. V., and Smirnov, A.: Satellite Ocean Aerosol Retrieval (SOAR)
Algorithm Extension to S-NPP VIIRS as Part of the "Deep Blue" Aerosol Project, J. Geophys. Res. Atmos, 123, 380–400,
https://doi.org/10.1002/2017JD027412, 2018.

Skamarock, W. C., Klemp, J. B., Dudhia, J., Gill, D. O., Liu, Z., Berner, J., and Huang, X.: NCAR Tech. Note NCAR/TN-556+STR: A
Description of the Advanced Research WRF Model Version 4, https://doi.org/10.5065/1dfh-6p97, 2019.

Skamarock, W. C. et al.: NCAR Tech. Note NCAR/TN-475+STR: A Description of the Advanced Research WRF Model Version 3,
https://doi.org/10.5065/D68S4MVH, 2008.

Stokes, R. H. and Robinson, R. A.: Interactions in Aqueous Nonelectrolyte Solutions. I. Solute-Solvent Equilibria, J. Phys. Chem., 70,
2126–2131, https://doi.org/10.1021/j100879a010, 1966.

Tao, Z., Yu, H., and Chin, M.: The Role of Aerosol-Cloud-Radiation Interactions in Regional Air Quality-A NU-WRF Study over the United
States, Atmosphere, 6, 1045–1068, https://doi.org/10.3390/atmos6081045, 2015.

Tegen, I., Hollrig, P., Chin, M., Fung, I., Jacob, D., and Penner, J.: Contribution of different aerosol species to the global aerosol extinction
optical thickness: Estimates from model results, J. Geophys. Res. Atmos., 102, 23 895–23 915, https://doi.org/10.1029/97JD01864, 1997.

Tiedtke, M.: A comprehensive mass flux scheme for cumulus parameterization in large-scale models, Mon. Weather. Rev., 117, 1779–1800,
https://doi.org/10.1175/1520-0493(1989)117<1779:ACMFSF>2.0.CO;2, 1989.

Wang, J., Wang, S., Jiang, J., Ding, A., Zheng, M., Zhao, B., Wong, D. C., Zhou, W., Zheng, G., Wang, L., Pleim, J. E., and Hao, J.: Impact
of aerosol-meteorology interactions on fine particle pollution during China's severe haze episode in January 2013, Environ. Res. Lett., 9,
https://doi.org/10.1088/1748-9326/9/9/094002, 2014a.

845   Wang, Q., Jacob, D. J., Spackman, J. R., Perring, A. E., Schwarz, J. P., Moteki, N., Marais, E. A., Ge, C., Wang, J., and Barrett, S. R. H.: Global budget and radiative forcing of black carbon aerosol: Constraints from pole-to-pole (HIPPO) observations across the Pacific, J. Geophys. Res. Atmos., 119, 195–206, https://doi.org/10.1002/2013JD020824, 2014b.

Wang, Y., Yuan, Q., Shen, H., Zheng, L., and Zhang, L.: Investigating multiple aerosol optical depth products from MODIS and VIIRS over Asia: Evaluation, comparison, and merging, Atmos. Environ., 230, 117 548, https://doi.org/10.1016/j.atmosenv.2020.117548, 2020.

850   Wiscombe, W. J.: NCAR Tech. Note, TN-140+STR: Mie scattering calculations: Advances in technique and fast, vector-speed computer codes, 1979.

Witte, M. K., Yuan, T., Chuang, P. Y., Platnick, S., Meyer, K. G., Wind, G., and Jonsson, H. H.: MODIS Retrievals of Cloud Effective Radius in Marine Stratocumulus Exhibit No Significant Bias, Geophys. Res. Lett., 45, 10,656–10,664, https://doi.org/10.1029/2018GL079325, 2018.

855   Wolke, R., Knoth, O., Hellmuth, O., Schröder, W., and Renner, E.: The parallel model system LM-MUSCAT for chemistry-transport simulations: Coupling scheme, parallelization and applications, Adv. Par. Com., 13, 363–369, https://doi.org/10.1016/S0927-5452(04)80048-0, 2004.

Wong, D. C., Pleim, J., Mathur, R., Binkowski, F., Otte, T., Gilliam, R., Pouliot, G., Xiu, A., Young, J. O., and Kang, D.: WRF-CMAQ two-way coupled system with aerosol feedback: software development and preliminary results, Geosci. Model. Dev., 5, 299–312, 860   https://doi.org/10.5194/gmd-5-299-2012, 2012.

Wong, J., Barth, M. C., and Noone, D.: Evaluating a lightning parameterization based on cloud-top height for mesoscale numerical model simulations, Geosci. Model Dev., 6, 429–443, https://doi.org/10.5194/gmd-6-429-2013, 2013.

Xing, J., Mathur, R., Pleim, J., Hogrefe, C., Gan, C.-M., Wong, D. C., Wei, C., and Wang, J.: Air pollution and climate response to aerosol direct radiative effects: A modeling study of decadal trends across the northern hemisphere, J. Geophys. Res. Atmos., 120, 12,221–12,236, 865   https://doi.org/10.1002/2015JD023933, 2015.

Yan, H., Huang, J., Minnis, P., Yi, Y., Sun-Mack, S., Wang, T., and Nakajima, T. Y.: Comparison of CERES-MODIS cloud microphysical properties with surface observations over Loess Plateau, J. Quant. Spectrosc. Ra., 153, 65–76, https://doi.org/10.1016/j.jqsrt.2014.09.009, 2015.

Yang, J., Li, J., Li, P., Sun, G., Cai, Z., Yang, X., Cui, C., Dong, X., Xi, B., Wan, R., Wang, B., and Zhou, Z.: Spatial Distribution and Impacts 870   of Aerosols on Clouds Under Meiyu Frontal Weather Background Over Central China Based on Aircraft Observations, J. Geophys. Res. Atmos., 125, e2019JD031 915, https://doi.org/10.1029/2019JD031915, 2020.

Yu, F. and Luo, G.: Simulation of particle size distribution with a global aerosol model: contribution of nucleation to aerosol and CCN number concentrations, Atmos. Chem. Phys., 9, 7691–7710, https://doi.org/10.5194/acp-9-7691-2009, 2009.

Yu, S., Mathur, R., Pleim, J., Wong, D., Gilliam, R., Alapaty, K., Zhao, C., and Liu, X.: Aerosol indirect effect on the grid-scale clouds in 875   the two-way coupled WRF-CMAQ: model description, development, evaluation and regional analysis, Atmos. Chem. Phys., 14, 11 247–11 285, https://doi.org/10.5194/acp-14-11247-2014, 2014.

Zaveri, R. A., Easter, R. C., Fast, J. D., and Peters, L. K.: Model for Simulating Aerosol Interactions and Chemistry (MOSAIC), J. Geophys. Res. Atmos., 113, https://doi.org/10.1029/2007JD008782, 2008.

Zender, C. S., Bian, H., and Newman, D.: Mineral Dust Entrainment and Deposition (DEAD) model: Description and 1990s dust climatology, 880   J. Geophys. Res. Atmos., 108, https://doi.org/10.1029/2002JD002775, 2003.

Zhang, C. and Wang, Y.: Projected future changes of tropical cyclone activity over the western North and South Pacific in a 20-km-Mesh regional climate model, J. Climate, 30, 5923–5941, https://doi.org/10.1175/JCLI-D-16-0597.1, 2017.

Zhang, C., Wang, Y., and Hamilton, K.: Improved representation of boundary layer clouds over the southeast Pacific in ARW-WRF using a modified Tiedtke cumulus parameterization scheme, Mon. Weather Rev., 139, 3489–3513, https://doi.org/10.1175/MWR-D-10-05091.1, 2011a.

Zhang, Q., Quan, J., Tie, X., Huang, M., and Ma, X.: Impact of aerosol particles on cloud formation: Aircraft measurements in China, Atmos. Environ., 45, 665–672, https://doi.org/10.1016/j.atmosenv.2010.10.025, 2011b.

Zhang, X., Zhang, Q., Hong, C., Zheng, Y., Geng, G., Tong, D., Zhang, Y., and Zhang, X.: Enhancement of PM2.5 Concentrations by Aerosol-Meteorology Interactions Over China, J. Geophys. Res. Atmos., 123, 1179–1194, https://doi.org/10.1002/2017JD027524, 2018.

Zhang, Y.: Online-coupled meteorology and chemistry models: history, current status, and outlook, Atmos. Chem. Phys., 8, 2895–2932, https://doi.org/10.5194/acp-8-2895-2008, 2008.

Zhang, Y., Wen, X.-Y., and Jang, C.: Simulating chemistry–aerosol–cloud–radiation–climate feedbacks over the continental U.S. using the online-coupled Weather Research Forecasting Model with chemistry (WRF/Chem), Atmos. Environ., 44, 3568 – 3582, https://doi.org/10.1016/j.atmosenv.2010.05.056, 2010.

Zhang, Y., Mao, H., Ding, A., Zhou, D., and Fu, C.: Impact of synoptic weather patterns on spatio-temporal variation in surface O-3 levels in Hong Kong during 1999-2011, Atmos. Environ., 73, 41–50, https://doi.org/10.1016/j.atmosenv.2013.02.047, 2013.

Zhang, Y., Zhang, X., Wang, L., Zhang, Q., Duan, F., and He, K.: Application of WRF/Chem over East Asia: Part I. Model evaluation and intercomparison with MM5/CMAQ, Atmos. Environ., 124, 285–300, https://doi.org/10.1016/j.atmosenv.2015.07.022, 2016.

Zhao, B., Liou, K.-N., Gu, Y., Li, Q., Jiang, J. H., Su, H., He, C., Tseng, H.-L. R., Wang, S., Liu, R., Qi, L., Lee, W.-L., and Hao, J.: Enhanced PM2.5 pollution in China due to aerosol-cloud interactions, Sci. Rep., 7, https://doi.org/10.1038/s41598-017-04096-8, 2017.

Zhao, C., Qiu, Y., Dong, X., Wang, Z., Peng, Y., Li, B., Wu, Z., and Wang, Y.: Negative Aerosol-Cloud r(e) Relationship From Aircraft Observations Over Hebei, China, Earth and Space Science, 5, 19–29, https://doi.org/10.1002/2017EA000346, 2018.

Zheng, G. J., Duan, F. K., Su, H., Ma, Y. L., Cheng, Y., Zheng, B., Zhang, Q., Huang, T., Kimoto, T., Chang, D., Poeschl, U., Cheng, Y. F., and He, K. B.: Exploring the severe winter haze in Beijing: the impact of synoptic weather, regional transport and heterogeneous reactions, Atmos. Chem. Phys., 15, 2969–2983, https://doi.org/10.5194/acp-15-2969-2015, 2015.
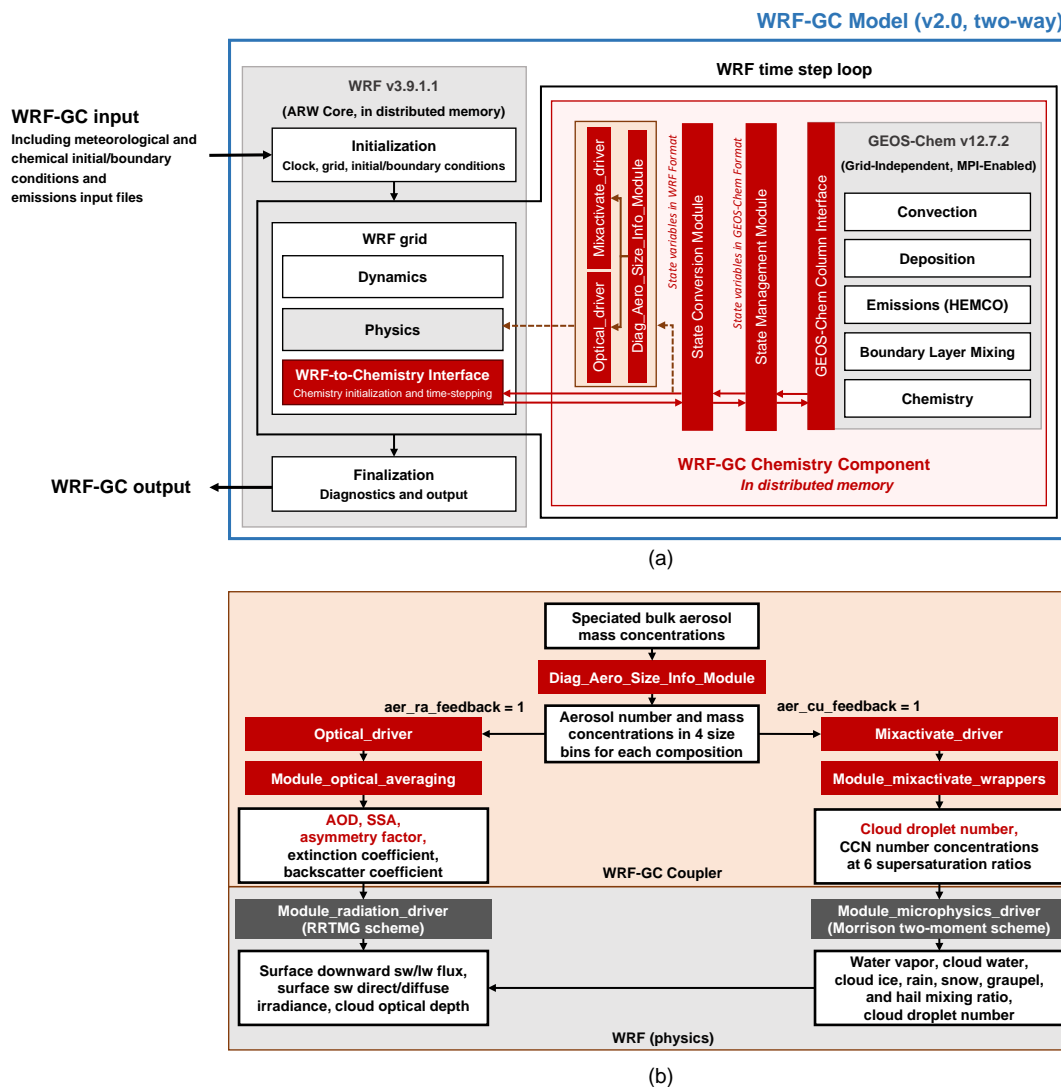
Figure 1. (a) Architectural overview of the WRF-GC coupled model (v2.0). The WRF-GC Coupler (all parts shown in red) includes interfaces to the two parent models, as well as the two-way coupling modules (shown in orange). The parent models (shown in grey) are standard codes downloaded from their sources, without any modifications. (b) flow diagram of the aerosol-radiation and aerosol-cloud interactions in two-way coupled WRF-GC model.
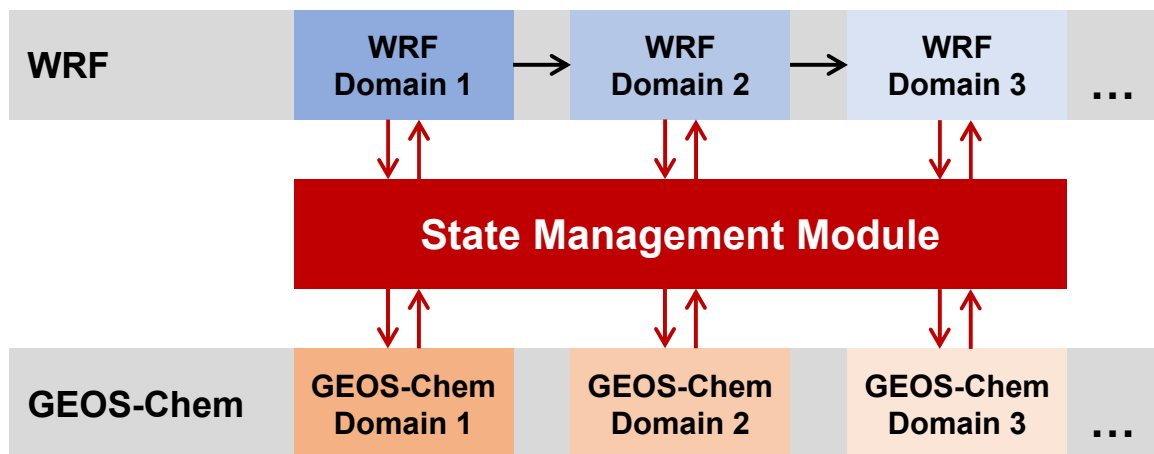
Figure 2. Illustration of the state management module operating in the nested-domain WRF-GC.
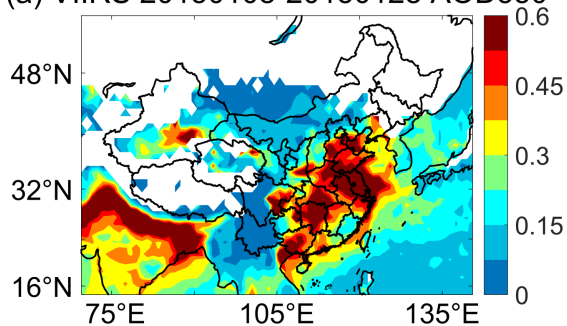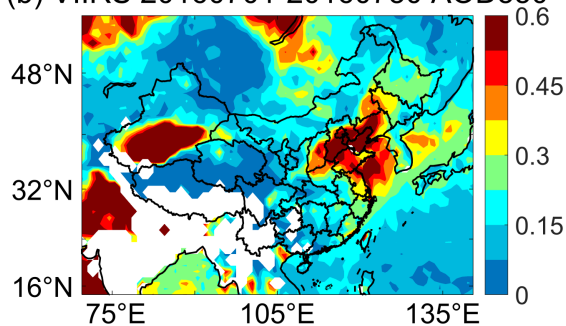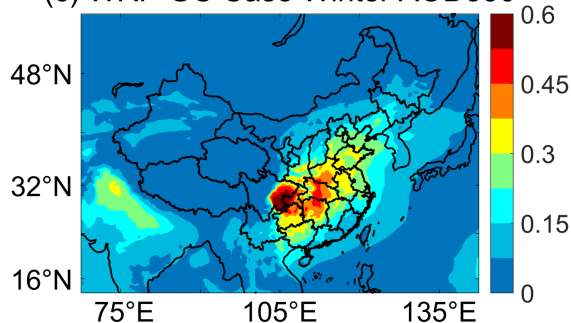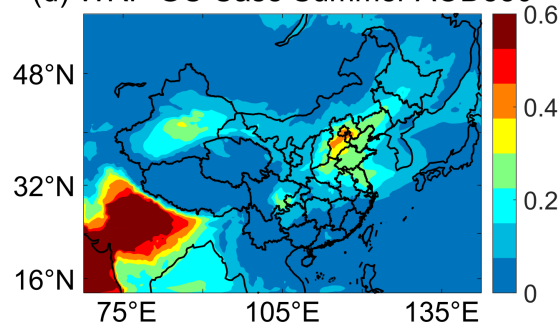
Figure 3. Spatial distributions of the time-averaged AOD at 550 nm during January 8 to January 28, 2015 from (a) VIIRS observations, and (c) Case Winter (WRF-GC v2.0); or during July 1 to July 30, 2016 from (b) VIIRS observations and (d) Case Summer (WRF-GC v2.0)
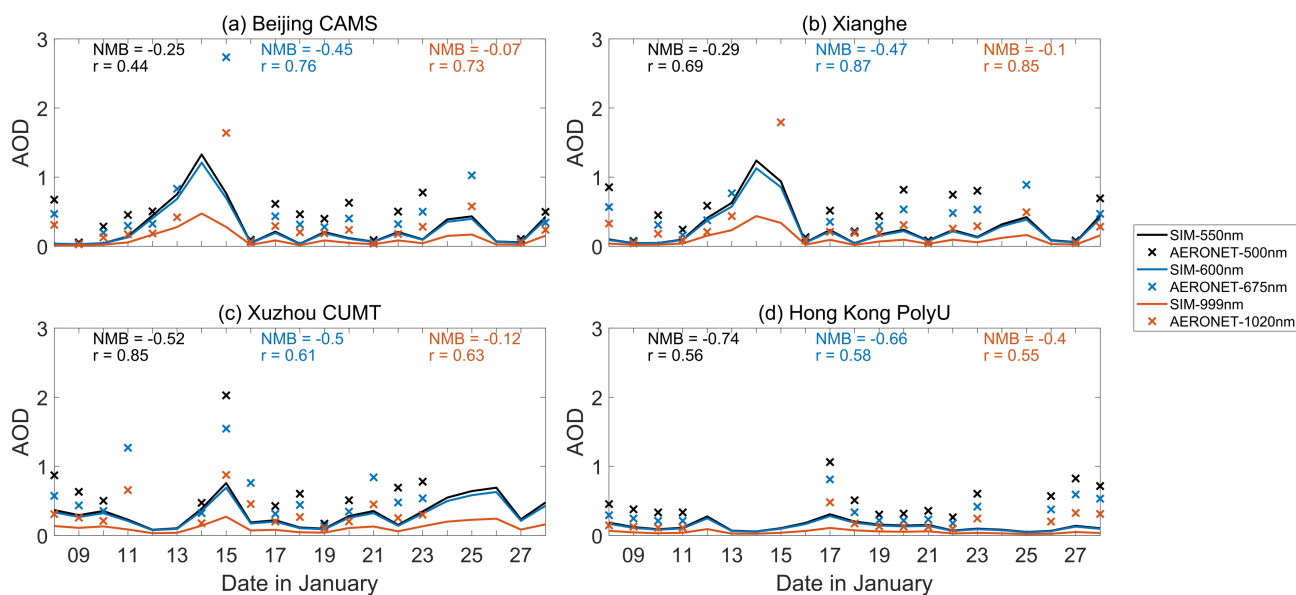
Figure 4. Simulated daily AOD (550 nm, 600 nm, 999 nm) from Case Winter against the observed AOD (500 nm, 675 nm, 1020 nm) from AERONET dataset during January 08 to January 28, 2015 at (a) Beijing CAMS, (b) Xianghe, (c) Xuzhou CUMT, and (d) Hong Kong PolyU
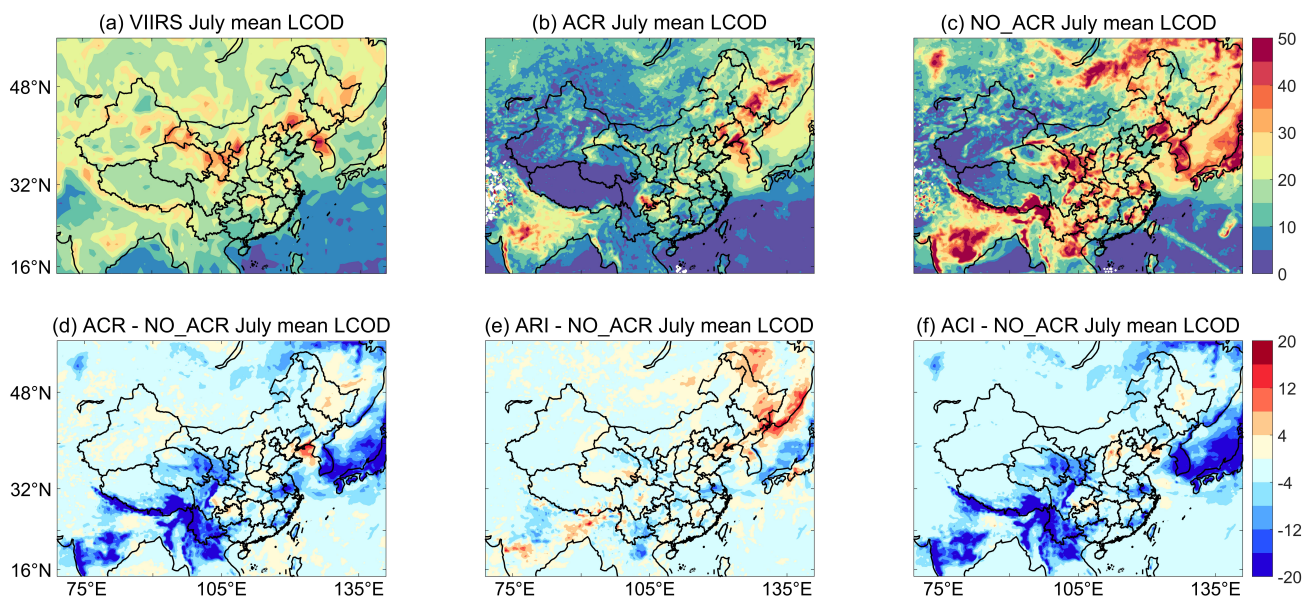
Figure 5. Monthly mean LCOD from (a) VIIRS observations, (b) the Case ACR simulation, and (c) the Case NO_ACR simulation during July, 2016. Differences of July mean LCOD between (d) the Case ACR and the Case NO_ACR, (e) the Case ARI and the Case NO_ACR, and (f) the Case ACI and the Case NO_ACR in 2016.
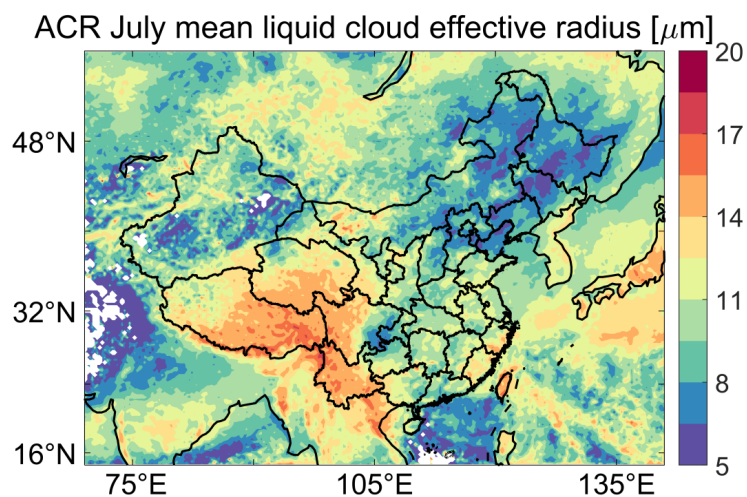
Figure 6. Monthly mean effective radii of liquid cloud from the Case ACR (Case Summer) simulation during July, 2016.
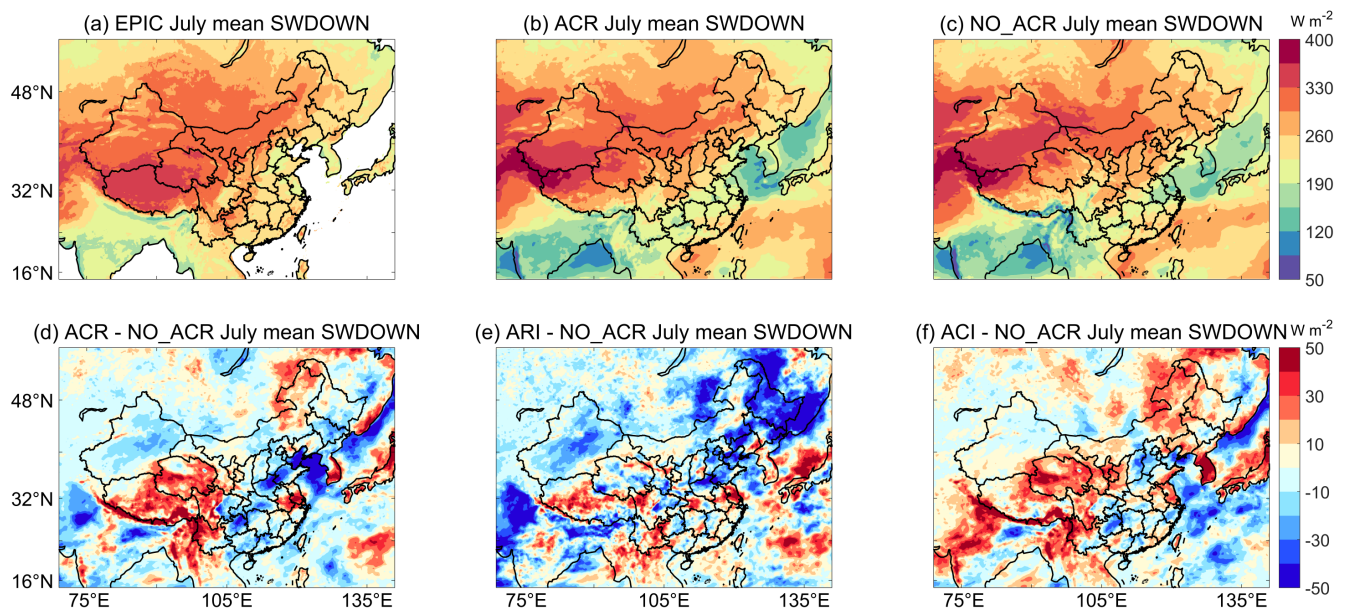
Figure 7. Monthly mean surface downward shortwave radiation from (a) EPIC observations, (b) the Case ACR simulation, and (c) the Case NO_ACR simulation during July, 2016. Differences of July mean surface downward shortwave radiation between (d) the Case ACR and the Case NO_ACR, (e) the Case ARI and the Case NO_ACR, and (f) the Case ACI and Case the NO_ACR in 2016.
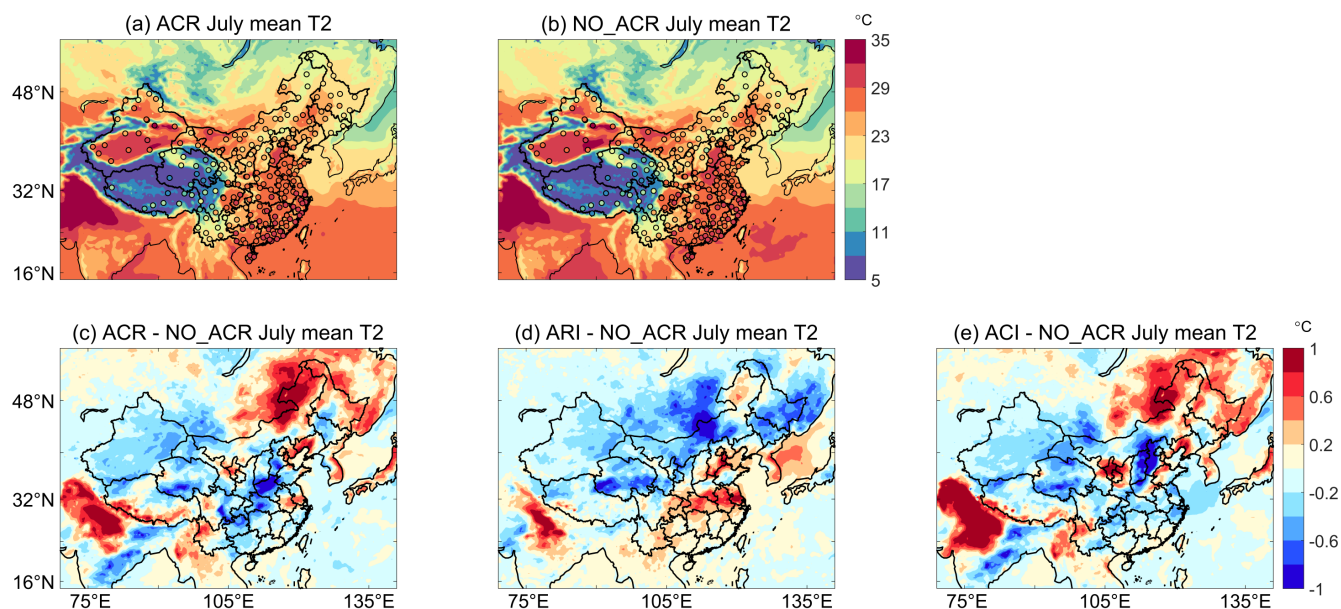
Figure 8. Comparison of the observed (filled symbols) and simulated (filled contours) monthly mean surface air temperature from (a) the Case ACR and (b) the Case NO_ACR. Differences of monthly mean surface air temperature between (c) the Case ACR and Case NO_ACR, (d) the Case ARI and the Case NO_ACR, and (e) the Case ACI and the Case NO_ACR during July 2016.
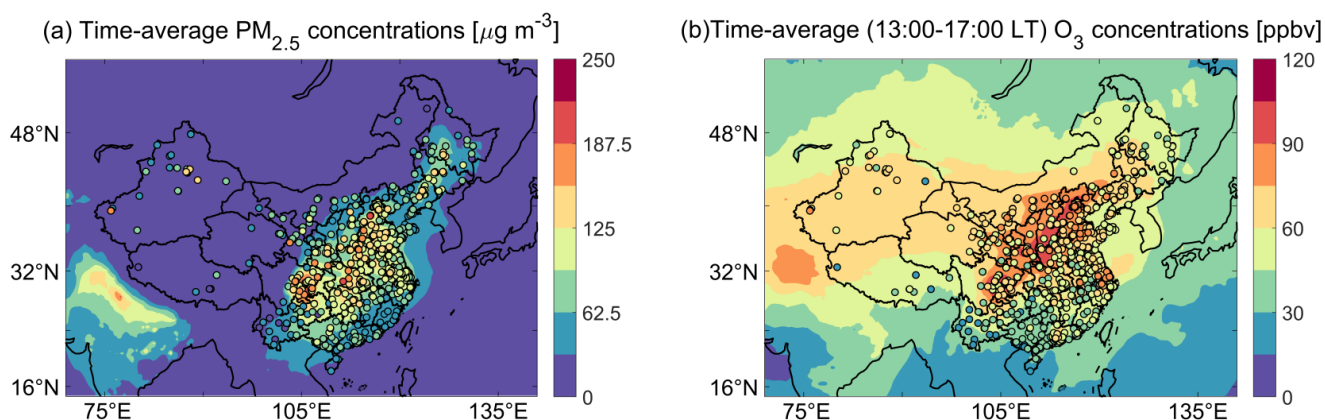
Figure 9. (a) Time-average $PM_{2.5}$ concentrations during Jan 8 to Jan 28 2015 from Case Winter simulation, and (b) Time-average afternoon ozone concentrations (13:00 to 17:00 local time) during July 1 to July 30 2016 from Case Summer simulation against the surface measurements managed by the Ministry of Ecology and Environment (MEE) of China.
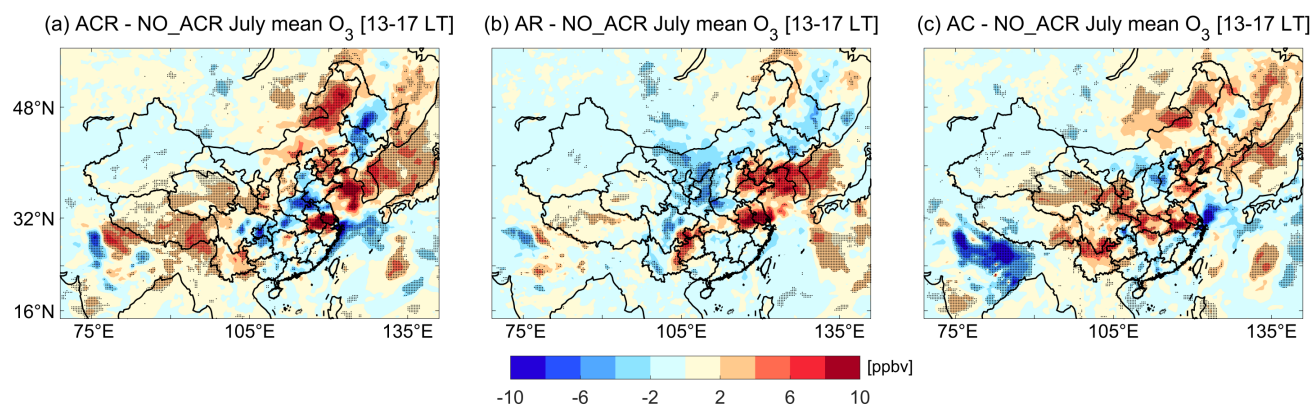
Figure 10. Differences of simulated monthly mean afternoon (13:00 to 17:00 local sun time) surface ozone concentrations during July 2016 (a) between the Case ACR and Case NO_ACR experiments, (b) between the Case ARI and Case NO_ACR experiments, and (c) between the Case ACI and Case NO_ACR experiments. Stippled grids represented significant differences (two-tail t-test at 5 % significance level).
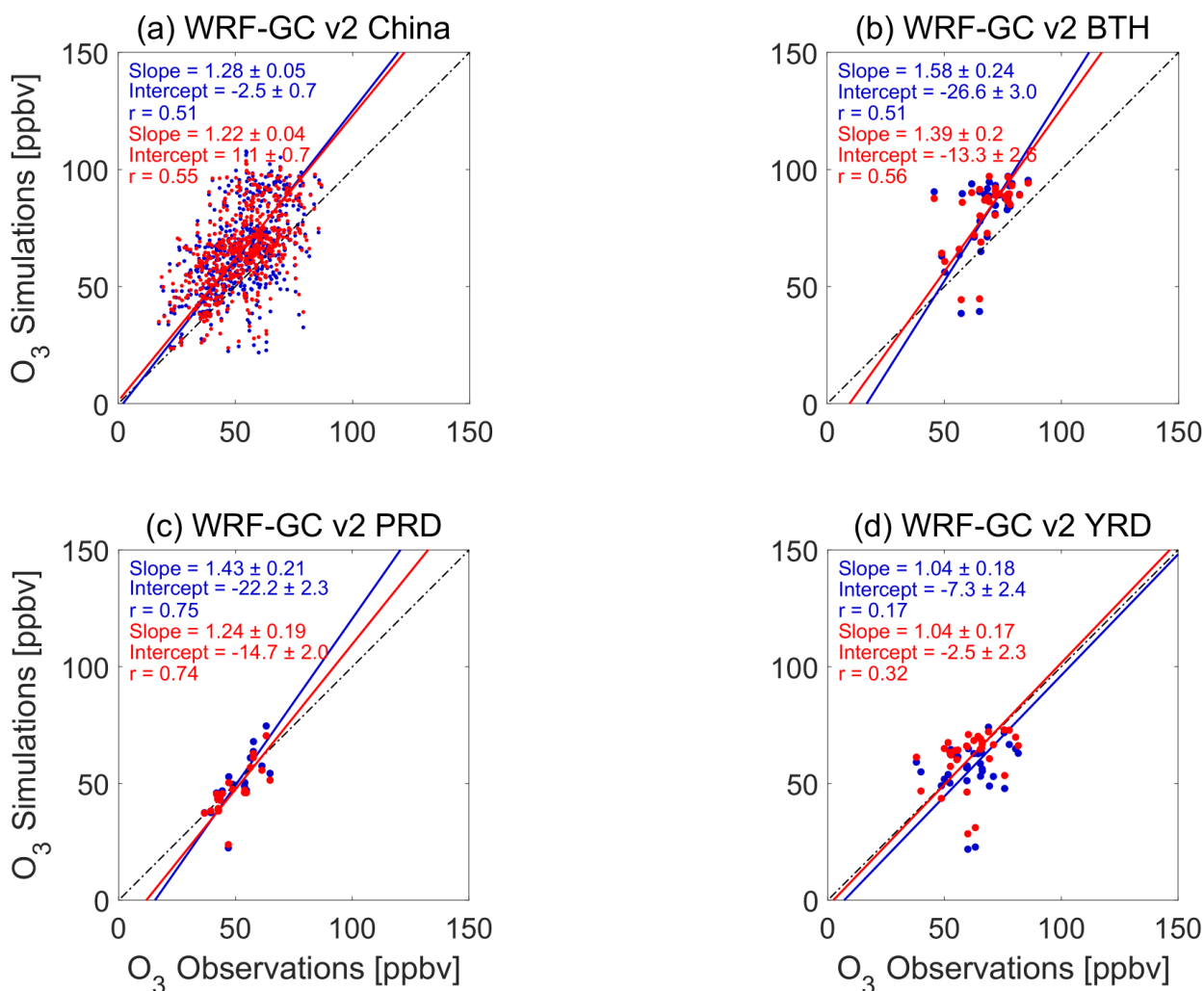
Figure 11. Comparison of the observed and simulated (Case ACR: red, Case NO_ACR: blue) monthly mean afternoon ozone concentrations during July, 2016 at (a) 581 sites over China, (b) 32 sites in the BTH area, (c) 20 sites in the PRD area, and (d) 32 sites in the YRD area. The correlation coefficients and the slopes and intercepts from reduced-major axis regression are shown inset. The dash-dotted lines indicate the 1:1 lines.

Table 1. Aerosol types in WRF-GC and their prescribed properties and size distributions

Name	Species	Molecular weight ($g \cdot mol^{-1}$)	Density ($g \cdot cm^{-3}$)	Hygroscopicity (unitless)	Log-normal distribution (Geometric mean dry diameter, μm)	Log-normal distribution (Geometric standard deviation, unitless)
SO4	sulfate	96	1.7	0.5	0.14	1.6
NIT	nitrate	62	1.8	0.5	0.14	1.6
NH4	ammonium	18	1.8	0.5	0.14	1.6
OCPI	hydrophilic primary OC	12	1.3	0.2	0.14	1.6
OCPO	hydrophobic primary OC	12	1.3	0.2	0.14	1.6
BCPI	hydrophilic BC	12	1.8	1.00E-06	0.04	1.6
BCPO	hydrophobic BC	12	1.8	1.00E-06	0.04	1.6
SALA	accumulation-mode sea salt (radius 0.1 - 0.5 μm)	31.4	2.2	1.16	0.18	1.5
SALC	coarse-mode sea salt (radius 0.5 - 4.0 μm)	31.4	2.2	1.16	0.8	1.8
DST1	dust bin 1 (radius 0.1 - 1.0 μm)	29	2.5	0.14	–	–
DST2	dust bin 2 (radius 1.0 - 1.8 μm)	29	2.65	0.14	–	–
DST3	dust bin 3 (radius 1.8 - 3.0 μm)	29	2.65	0.14	–	–
DST4	dust bin 1 (radius 3.0 - 6.0 μm)	29	2.65	0.14	–	–
SOAS	SOA (simple)	150	1.5	0.14	0.14	1.6

Table 2. Upper and lower bounds of particle dry diameter for the 4 size bins used by WRF-GC

Bin	Lower bound (μm)	Upper bound (μm)
1	0.0390625	0.15625
2	0.15625	0.625
3	0.625	2.5
4	2.5	10.0

Table 3. WRF-GC model configurations of experiments

Experiment	Case Winter	Case ACR (Case Summer)	Case ARI	Case ACI	Case NO_ACR
Simulation time (UTC)	2015-01-04 00Z to 2015-01-29 00Z	2016-06-27 00Z to 2016-07-31 00Z			
Microphysics	Morrison two-moment (Morrison et al., 2009)				
Shortwave radiation	RRTMG (Iacono et al., 2008)				
Longwave radiation	RRTMG (Iacono et al., 2008)				
Planetary boundary layer	YSU (Hong et al., 2006)				
Land Surface	Noah (Chen and Dudhia, 2001a, b)				
Surface layer	MM5 Monin-Obukhov (Jimenez et al., 2012)				
Cumulus parameterization	New Tiedtke (Tiedtke, 1989; Zhang et al., 2011a; Zhang and Wang, 2017)				
Aerosol-radiation interaction	On	On	On	Off	Off
Aerosol-cloud interaction	On	On	Off	On	Off